Materials and Structures (2026) 59:333
https://doi.org/10.1617/s11527-026-03216-z

ORIGINAL ARTICLE

Nanostructure and chemistry of amorphous Al-rich C-(N)-A-S–H-type gels via aqueous precipitation: insights for alkali-activated materials

Farnaz Aghabeyk · Boyu Chen · Mayank Gupta · Chen Liu · Guang Ye

Received: 11 March 2026 / Revised: 17 July 2026 / Accepted: 21 July 2026

Abstract Calcium-sodium aluminosilicate hydrate (C-(N)-A-S–H) gels are the primary phases in alkali-activated slag (AAS) systems and govern paste-scale microstructural evolution. Conventional models assume cross-linked and non-cross-linked C-(N)-A-S–H gels with Ca/(Si + Al) > 0.67 and Al/Si < 0.25. However, several studies have reported Al-rich gels (Al/Si > 0.25) in both AAS and in alkali-activated blends with lower calcium content, whose nanostructure and chemistry remain insufficiently resolved. In this study, four amorphous Al-rich C-(N)-A-S–H gels spanning Al/Si = 0.31–0.57 and Ca/Si = 0.56–1.04 were synthesized to enable two orthogonal comparisons: (i) varying Al/Si at constant Ca/Si to isolate Al-for-Si substitution effects, and (ii) varying Ca/Si at constant Al/Si to probe calcium role on network connectivity. Comprehensive characterization revealed the coexistence of local structural environments characteristic of C-(N)-A-S–H/C-A-S–H, (N,C)-A-S–H, and N-A-S–H-like gel domains without the formation of crystalline secondary phases. ^{29}Si NMR revealed a progressive increase in Q^4(mAl)-rich sites with increasing Al incorporation, while the relative proportion of the C-(N)-A-S–H/C-A-S–H environments decreased with decreasing Ca/Si ratio. ^{27}Al NMR confirmed tetrahedral Al coordination, with chemical shifts varying with Ca/Si ratio, reflecting changes in interlayer charge-balancing. Octahedral Al was detected exclusively in gels with a higher Al/Si at 0.5, indicating the formation of more highly polymerized aluminosilicate environments under high-Al conditions. ^{23}Na NMR revealed chemical shifts of − 5.81 to − 6.21 ppm, correlating strongly with the Na/Al ratio. Collectively, the findings demonstrate that gels with Al/Si > 0.25 deviate from classical tobermorite-like structures and exhibit increasingly polymerized and structurally heterogeneous aluminosilicate environments.

Supplementary Information The online version contains supplementary material available at https://doi.org/10.1617/s11527-026-03216-z.

F. Aghabeyk (✉) · B. Chen · C. Liu
Microlab, Section Materials and Environment, Faculty of Civil Engineering and Geosciences, Delft University of Technology, Stevinweg 1, 2628 CN Delft, The Netherlands
e-mail: F.Aghabeyk@tudelft.nl

B. Chen
e-mail: B.Chen-4@tudelft.nl

C. Liu
e-mail: c.liu-12@tudelft.nl

M. Gupta · G. Ye (✉)
Numerical Modeling and Digitization of Building Materials and Concrete Structures, The Karlsruhe Institute of Technology, Kaiserstraße 12, 76131 Karlsruhe, Germany
e-mail: G.Ye@tudelft.nl

M. Gupta
e-mail: mayank.gupta@kit.edu

Published online: 06 August 2026

Highlights

- Synthesis of Al-rich C-(N)-A-S-H gels (Al/Si > 0.25) via aqueous precipitation
- XRD confirmed all gels form poorly crystalline C-S-H-like structure
- Al enrichment did not promote crystallization of secondary phases
- ^{29}Si NMR revealed the coexistence of multiple gels
- BET confirmed microporous gels with surface areas 67–199 m^2/g

Keywords C-(N)-A-S–H gel · ^{23}Na · ^{27}Al and ^{29}Si NMR · Alkali-activated materials · Al/Si ratio

Abbreviations

C-S-H	Calcium silicate hydrate gel
C-A-S-H	Calcium aluminosilicate hydrate gel
N-A-S-H	Sodium aluminosilicate hydrate gel
(N,C)-A-S-H	Ca-containing, sodium aluminosilicate hydrate gel
C-(N)-A-S-H	Alkali charge-balanced, aluminum-substituted calcium silicate hydrates gel
Al-rich C-(N)-A-S-H	C-(N)-A-S–H gels with Al/Si ratios > 0.25; aluminosilicate hydrate gel studied in this work
AAM	Alkali-activated materials
AAS	Alkali-activated slag system
AASB	Alkali-activated slag-blended system
AAB	Alkali-activated blended system

1 Introduction

The production of Portland Cement (PC) is highly resource- and energy-intensive, contributing approximately 8% of global CO_2 emissions [1, 2]. To mitigate the environmental impact of cement production, alkali-activated materials (AAMs) have emerged as a promising alternative [3–5]. These environmentally friendly materials are produced by reacting to an aluminosilicate-rich precursor with an alkaline activator [6]. So far, various industrial by-products have been explored as potential precursors in AAMs [7]. This approach offers a dual benefit: reducing the carbon footprint caused by cement production and addressing waste disposal challenges for industrial by-products.

The use of precursors in AAMs, however, has largely remained limited to conventional materials, such as GGBFS and coal fly ash, both of which face growing limitations in availability [8, 9]. To address this limitation, researchers have explored the use of alternative residues, such as municipal solid waste incineration (MSWI) bottom ash [10–12], or biomass ash [13], in alkali-activated blended (AAB) systems. In these AAB systems, at least two solid precursors are co-activated, providing an opportunity to utilize industrial residues as precursors while potentially enhancing the overall performance of AAMs [14]. However, the use of multiple precursors inherently increases the complexity of the microstructure compared to alkali-activated single systems (one precursor), particularly when incorporating different industrial by-products as alternative precursors.

The reaction products formed within AAMs are critical in governing the microstructure, directly influencing their fresh and hardened properties [15, 16]. Reaction products in AAMs are classified as primary and/or secondary phases [17]. Primary phases are mainly dependent on the calcium content of precursors [6, 14] while the formation of secondary phases, such as hydroxides or zeolites, is influenced by the availability of aluminum in the composition of precursors [18]. In high-Ca systems, the primary phase can be calcium aluminosilicate hydrate (C-A-S–H) or calcium–sodium aluminosilicate hydrate (C-(N)-A-S–H) gels, while in low-Ca systems, the primary phase is sodium aluminosilicate hydrate (N-A-S–H) gel [6, 19–21].

In intermediate-Ca systems, the chemical complexity increases significantly compared to the low-Ca and high-Ca systems [20]. In these systems, intermediate gel phases form, which are often described as a combination of C-A-S–H and Ca-containing N-A-S–H (referred to as (N,C)-A-S–H) gels [20, 22]. However, according to the literature, this classification may oversimplify the intermediate system, as a wider range of coexisting gel phases has been observed. Several studies have indicated that intermediate gels

may form through various combinations of C-(N)-A-S–H and N-A-S–H [23], C-(N)-A-S–H and C-A-S–H [24], C-A-S–H and N-A-S–H [5], or (N,C)-A-S–H and N-A-S–H [25] gels. These findings reveal that limiting the classification of intermediate gels to C-A-S–H and (N,C)-A-S–H may underestimate the chemical diversity and complexity of gel assemblages that develop under varying precursor and activation conditions.

C-(N)-A-S–H gel is widely regarded as the primary reaction product and main strength-giving phase in high-Ca AAMs, particularly in alkali-activated slag (AAS) systems [26]. This gel is known to form within a bulk compositional range of Al/Si < 0.25 and $0.67 \leq Ca/(Si + Al) \leq 1.2$ in AAS [1, 21, 26], and is broadly classified into non-cross-linked or cross-linked structures, depending on its aluminum content [26]. Despite this conventional understanding, several studies have reported the formation of C-(N)-A-S–H gels in AAS with substantially high Al/Si ratios (> 0.25), based on SEM–EDS analyses [27–34]. Interestingly, this high Al/Si ratio aligns more closely with the typical composition of N-A-S–H gel in low-Ca systems, which is characterized by Si/Al ratios below 3 (or Al/Si > 0.33) [35, 36]. Given the structural differences between tobermorite-like C-(N)-A-S–H [19] and 3D-network N-A-S–H gels [36], the structure of these Al-rich C-(N)-A-S–H gels, formed in AAS, remains unclear, limiting our understanding of their influence on the properties of AAS systems.

Beyond AAS systems, the formation of C-(N)-A-S–H gel in alkali-activated blended systems has been reported to be significantly more complex. For instance, the reaction products in alkali-activated slag blended (AASB) systems can range from a single-phase C-(N)-A-S–H gel to the coexistence of C-A-S–H and N-A-S–H gels, along with secondary phases [37]. Several studies have reported that, in AASB systems, SEM–EDS analyses reveal either the presence of C-(N)-A-S–H gels or the coexistence of C-A-S–H and N-A-S–H gels, typically characterized by Ca/Si < 0.8 and Al/Si > 0.25 [5, 28, 30, 38, 39]. This chemical composition for C-(N)-A-S–H gel is not limited to the SEM–EDS analysis of AASB; similar compositions have also been reported for C-(N)-A-S–H gels, formed in other blended systems, including binders incorporating phosphate sludge and waste glass [40], as well as alkali-activated metakaolin and limestone pastes [25]. The widespread formation of these high-Al C-(N)-A-S–H gels (Al/Si > 0.25) across different AAMs highlights the need for deeper investigation into their chemical composition and nanostructural characteristics.

Synthesizing the reaction products within AAMs has become a popular approach to understanding the chemistry and nanostructure of gels. Many studies have focused on the synthesis of C-A-S–H [41–43], N-A-S–H [3, 35, 44, 45], C-(N)-A-S–H [19, 46] or blends of C-(N)-A-S–H/C-A-S–H and N-A-S–H gels [1, 21, 47] to better understand the phase evolution and structural properties of these gels. The roles of Al and Ca in the C-(N)-A-S–H nanostructure have been studied using techniques such as MAS NMR [19, 46]. Higher bulk Ca content has been found to increase structural order, reduce cross-linking, and promote Ca–OH and AFm-type phase formation. In contrast, higher Al content leads to increased Al substitution, cross-linking, disorder, and the formation of Al^{V}, as well as Al-rich N-A-S–H gel formation [19, 46]. While these studies have significantly advanced our understanding of C-(N)-A-S–H gel nanostructure, they have primarily focused on limited conventional compositional ranges.

To date, most studies on synthetic gels have focused on non-cross-linked or cross-linked C-(N)-A-S–H gels with Al/Si ratios ≤ 0.25 in AAS systems [1, 19, 21, 46]. Research on synthesizing pure C-(N)-A-S–H gels with higher Al/Si ratios, resembling those of AAS and blended binder systems (AAB in general or AASB), remains limited. The only known study on Al-rich C-(N)-A-S–H gels reported difficulties in achieving amorphous gels, primarily due to the persistence of unreacted gibbsite and the formation of secondary carbonated phases like calcite [48].

The primary aim of this study is to advance the current understanding of Al-rich C-(N)-A-S–H gels in AAMs when incorporated with precursors of varying chemical compositions. Specifically, we have designed Al-rich C-(N)-A-S–H gels with Al/Si ratios exceeding the typical threshold of 0.25 for tobermorite-like C-(N)-A-S–H gels. This composition was selected to reflect high-aluminum C-(N)-A-S–H phases, as identified in the literature through SEM–EDS analysis (Fig. 1). A combination of analytical techniques, including X-ray fluorescence (XRF), X-ray diffraction (XRD), thermogravimetric analysis (TGA), Fourier-transform

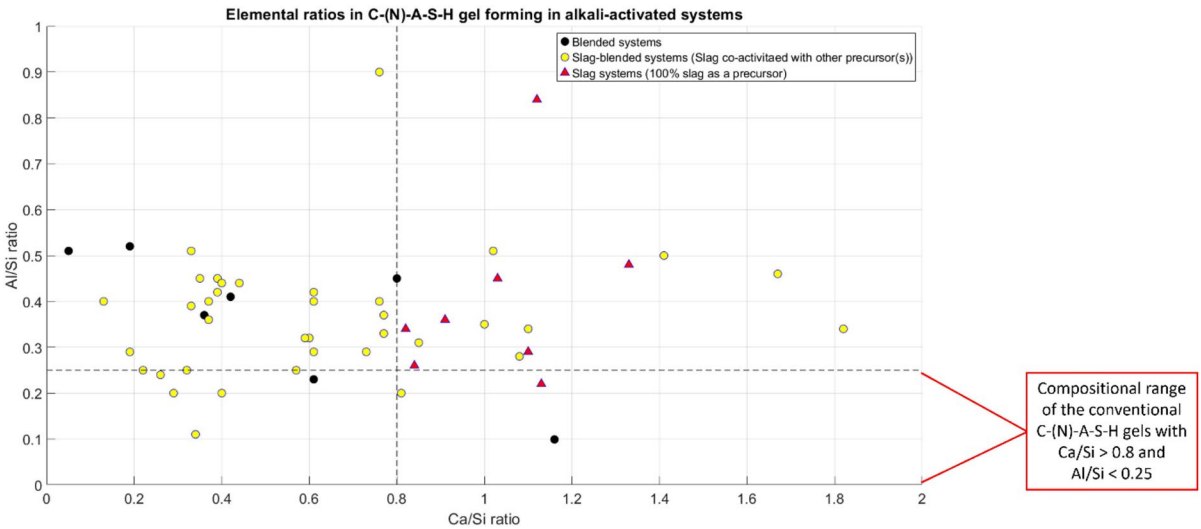

Fig. 1 Elemental ratios (Ca/Si vs. Al/Si) in C-(N)-A-S–H gels, derived from SEM–EDS analyses of alkali-activated systems reported in the literature (See Tables A.1 and A.2, Appendix A). The dashed lines represent the conventional compositional boundaries for C-(N)-A-S–H gels (Ca/Si > 0.8 and Al/Si < 0.25) and data points show the composition of C-(N)-A-S-Hs gel in various systems: blended (co-activation of two or more precursors), slag-blended (slag co-activated with other precursor(s)), and slag systems (100% slag activated as a single precursor). The wide distribution of gels, especially of those with Al/Si > 0.25, reflects the presence of Al-rich C-(N)-A-S–H gel phases beyond traditional classifications

infrared spectroscopy (FTIR), nuclear magnetic resonance (NMR), and Brunauer–Emmett–Teller (BET) surface area analysis, has been used to investigate the chemical and physical properties of the Al-rich C-(N)-A-S–H gels. The findings of this study are expected to significantly enhance the understanding of Al-rich C-(N)-A-S–H gels as primary phases and provide critical insights into their nanostructural characteristics.

2 Materials and methods

2.1 Synthesis of the Al-rich C-(N)-A-S–H gels

The synthesis of Al-rich C-(N)-A-S–H gels was conducted using an aqueous precipitation method. Solutions of $Ca(NO_3)_2 0.4H_2O$, $Al(NO_3)_3 0.9H_2O$, Na_2SiO_3, and NaOH were prepared 24 h in advance to synthesize gels. As shown in Table 1, all concentrations were kept constant, but solution volumes were systematically adjusted to achieve the targeted Ca/Si and Al/Si ratios: Ca/Si < 0.8 and Al/Si > 0.25 for the three representative gels in the blended system and one gel with Ca/Si > 0.8 and Al/Si > 0.25 as a reference gel for AAS. The bulk chemical compositions determined by XRF analysis are summarized in Table 2. It should be noted that the oxide weight percentages are normalized to 100 wt.%, as standard XRF analysis does not quantify light elements (H, C, N) or bound water. Molar ratios (Ca/Si, Al/Si, Na/Si) were calculated from the normalized oxide compositions.

As shown in Table 2, the reference gel (C1.0_A0.3) composition falls within the Ca/(Si + Al) range commonly reported for C-(N)-A-S–H gels in AAS ($0.67 \leq Ca/(Si + Al) \leq 1.0$) [1, 21, 26]. This gel, however, was intentionally synthesized to be Al-rich (Al/Si > 0.25) to replicate the compositional characteristics of "Al-rich" C-(N)-A-S–H gels identified in AAS via SEM–EDS analyses reported in the literature (Fig. 1). The remaining gel compositions extend toward lower Ca/(Si + Al) values (≤ 0.67), enabling the assessment of increasing Al content under reduced Ca availability, as discussed earlier for the blended systems. It is important to note that the selected gel compositions in this study are not intended to represent the full compositional range shown in Fig. 1, but rather to evaluate how elevated Al/Si ratios influence

the formation and nanostructure of C-(N)-A-S–H gels under varying Ca availability.

Moreover, the Na/Al (0.39–1.95) ratios obtained in this study are comparable with the reported range for synthetic C-(N)-A-S–H gels in the literature, where compositions were designed and evaluated based on their Ca/Si and Al/Si ratios [21, 46]. In addition, the high alkalinity of the synthesis solution (pH 13.94–14.13) is consistent with the pore solution chemistry typically observed in AAMs [46, 49].

The mixtures were constantly stirred under sealed conditions for 2 days under controlled ambient conditions, followed by centrifugation (Fig. 2) and washing with deionized water and absolute ethanol, as described in earlier work [46]. The synthetic gels were then freeze-dried using a BioBase freeze dryer operating at -80°C. The freeze-drying process was chosen over conventional drying methods to minimize alterations in the molecular structure of gels and to avoid carbonation that could compromise the accuracy of subsequent analyses [44, 50]. The freeze-drying process consisted of two steps: pre-freezing and vacuum drying. The gels were pre-frozen for 4–6 h, followed by vacuum drying for 24 h until complete desiccation. The dried gels were then stored in a Bel-Art™ Secador™ gas-purge desiccator cabinet under controlled relative humidity (< 10%) to further prevent carbonation.

2.2 Characterization techniques

The synthesis and subsequent centrifugation of Al-rich C-(N)-A-S–H gels result in two phases: an aqueous and a solid phase. For the aqueous phase, the pH value was determined through titration with 0.1 mol/L of HCl acid to ensure that values are comparable to the pore solution pH in AAMs [46]. After drying, the solid phase of the gels was characterized by multiple complementary analytical techniques (Fig. 2).

The chemical composition of gels was analyzed using a Panalytical Axios Max WD-XRF spectrometer. XRD phase identification was performed with a Bruker D8 Advance diffractometer, equipped with Bragg–Brentano geometry and a Lynxeye position-sensitive detector. Coupled θ–2θ scans were conducted over a range of 5° to 110° 2θ with a step size of 0.04° 2θ.

TGA, FTIR, BET, and ^{29}Si, ^{27}Al, and ^{23}Na MAS NMR spectroscopy were then conducted to assess structural properties. TGA was performed using a NETZSCH STA 449 F3 Jupiter® instrument. For this test, approximately 6–8 mg of each sample was

Table 1 Optimized volume and concentration of reagents and precursors for the synthesis of reaction products

Gels Labels	NaOH		Na_2SiO_3		$Al(NO_3)_2.9H_2O$		$Ca(NO_3)_2.4H_2O$		pH*
	Volume (ml)	Concentration (M)	Volume (ml)	Concentration (M)	Volume (ml)	Concentration (M)	Volume (ml)	Concentration (M)	
C1.0_A0.3	25	10	40	0.60	90	0.12	40	0.24	13.94
C0.7_A0.5	20	10	40	0.60	90	0.12	20	0.24	13.98
C0.7_A0.3	25	10	50	0.60	60	0.12	20	0.24	14.08
C0.5_A0.5	25	10	40	0.60	60	0.12	10	0.24	14.13

* The pH of the aqueous solution is calculated after centrifugation through titration as described in Sect. 2.2

Table 2 Chemical composition of the Al-rich C-(N)-A-S–H gels in wt.% and the calculated nominal molar ratios as determined by XRF

Gel name	CaO	SiO_2	Al_2O_3	Na_2O	Ca/(Al + Si)	Al/Si	Ca/Si	Na/Al
C1.0_A0.3	39.16	40.18	10.74	9.92	0.79	0.31	1.04	1.52
C0.7_A0.5	29.82	43.89	21.29	5.00	0.46	0.57	0.73	0.39
C0.7_A0.3	27.96	42.44	13.52	16.02	0.51	0.38	0.71	1.95
C0.5_A0.5	23.40	44.82	19.93	11.85	0.37	0.52	0.56	0.98

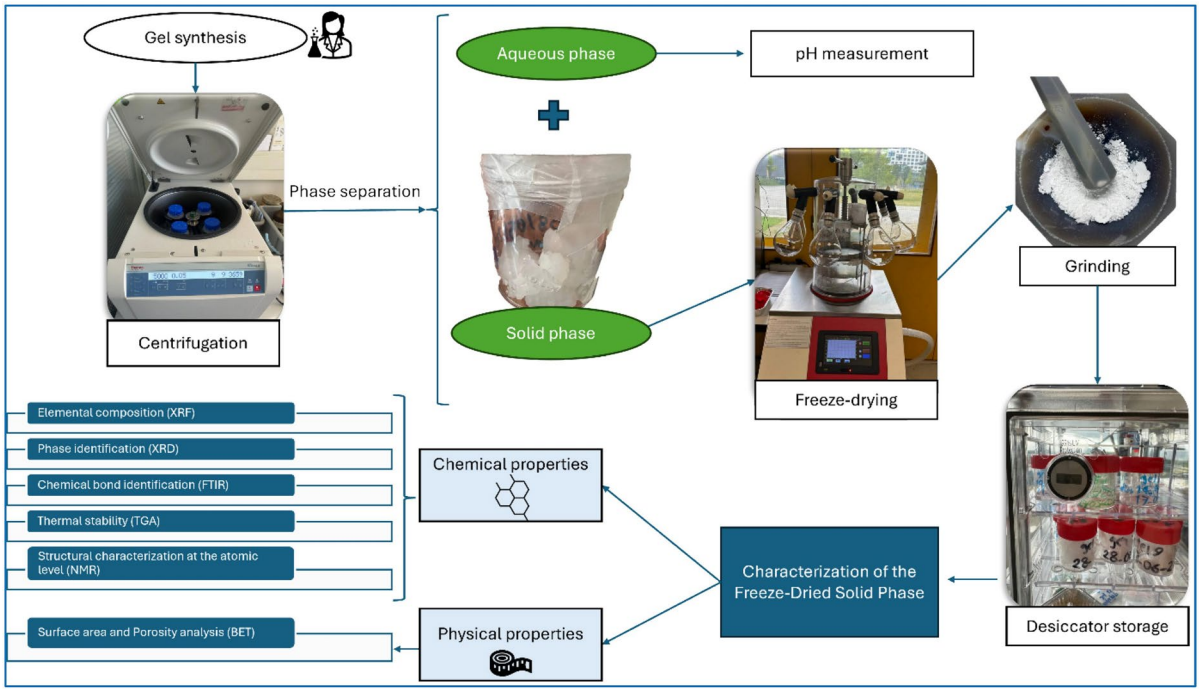

Fig. 2 Workflow for the synthesis, separation, and characterization of Al-rich C-(N)-A-S–H gels

heated from 40°C to 1000°C at a heating rate of 10°C/min under an argon atmosphere. FTIR spectra were acquired using a Nicolet™ iS50 FTIR spectrometer. The specific surface area and porosity of the gels were determined through BET analysis using Micromeritics Gemini VII 2390 V1.03.

^{29}Si NMR spectroscopy was conducted using a Bruker Avance Neo spectrometer equipped with a 500 MHz magnet. The MAS frequency was set to 20 kHz to minimize anisotropic interactions. A double-resonance H-F-X probe with a 3.2 mm rotor was employed, ensuring proper alignment at the magic angle (54.74°). A single-pulse excitation sequence was used, with an excitation pulse duration of 2 µs for the C0.7_A0.5 gel, while for the other gels, it was set to 3 µs. These different durations reflect independent per-sample calibration of the pulse length to ensure equivalent π/2 (90°) flip angles for each gel. A relaxation delay of 30 s was applied between scans to ensure complete relaxation. To increase the signal-to-noise ratio, a total of 5120 scans were acquired for C0.7_A0.5, C0.7_A0.3, and C0.5_A0.5, while 2663 scans were performed for the C1.0_A0.3. The deconvolution of the ^{29}Si NMR spectra was conducted using MestReNova (Mnova) software.

The ^{27}Al and ^{23}Na NMR spectra were acquired using a spinning frequency of 20 kHz, with a total of 1800 scans and a relaxation delay of 2 s. Chemical shift calibration was conducted using $Al(NO_3)_3$, NaCl, and tetramethylsilane (TMS) as reference standards.

3 Results and discussion

3.1 Chemical properties

3.1.1 XRD analysis

The XRD patterns of the synthetic gels are presented in Fig. 3. The patterns exhibit a poorly crystalline C-S–H-like structure, consistent with PDF# 00–034-0002, assigned to tobermorite (C-S–H (I)-like phase). This is characterized by broad humps at 2θ ≈ 29°, 32°, 49.6°, and 55° [51]. These patterns align with what is referred to as C-S–H (I), a tobermorite-like structure typically observed in C-S–H gels with Ca/Si ratios below 1.5 [52]. Importantly, the diffraction patterns associated with tobermorite-like structure are not limited to C-S–H gels [53]. Similar patterns have

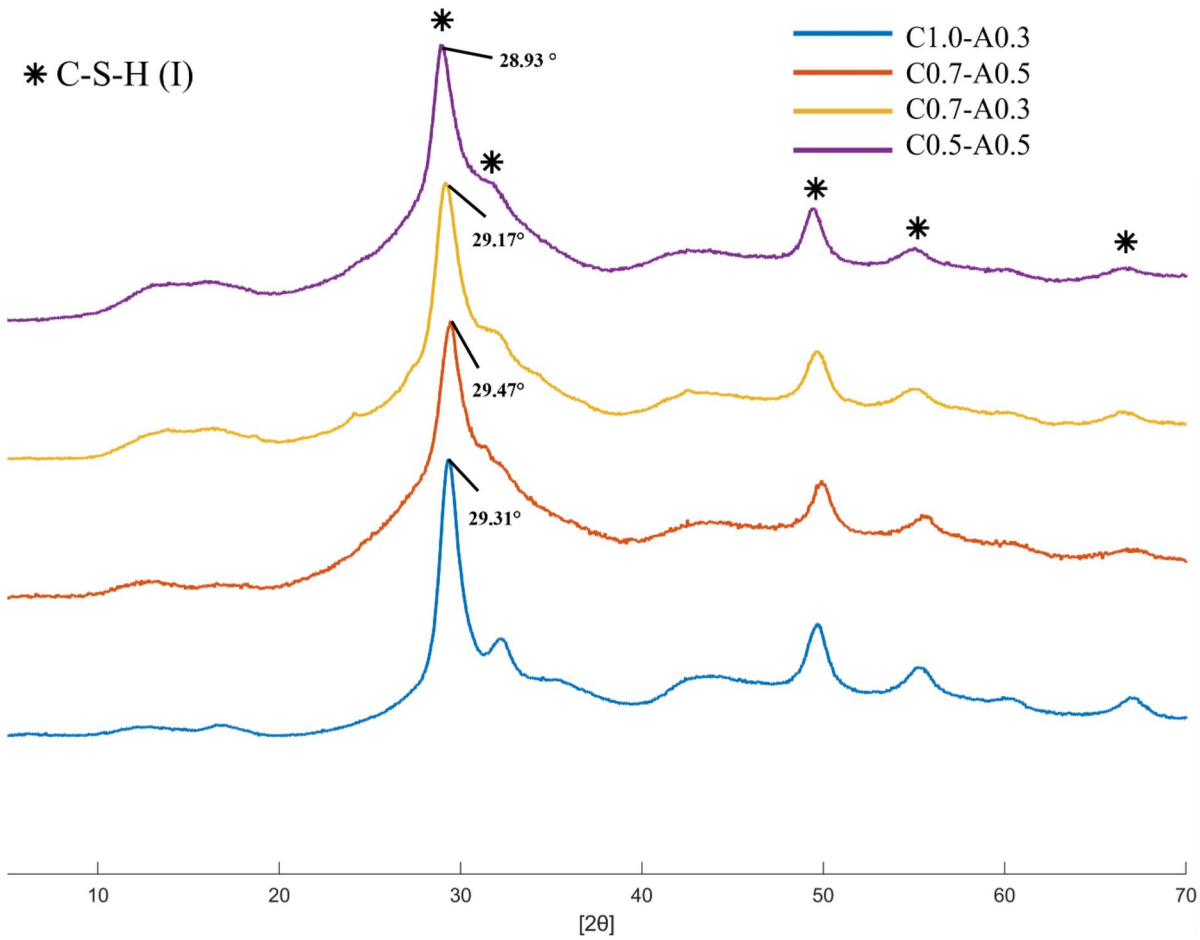

Fig. 3 XRD spectra of the synthetic gels with different molar ratios. Data are normalized to maximum intensity. * Represents the C-S–H (I)-like structure

also been reported in the XRD patterns of other gels, including C-A-S–H [42], blended C-(N)-A-S–H/N-A-S–H gels [21], and even alkali-silica gels [53, 54], as reported in the literature. However, the gel compositions in all those studies had relatively low Al/Si ratios (< 0.2). In contrast, although the Ca/Si ratio of the synthesized Al-rich C-(N)-A-S–H gels in this work falls within the typical range associated with the C-S–H (I) structure, their significantly higher Al/Si ratio (> 0.3) indicates that tobermorite-like gel structures can also persist in Al-rich systems. Moreover, this finding can further indicate that the phase reported as C-S–H (I) in AAS [55–57] and AASB [58, 59] systems may, in some cases, correspond to Al-rich C-(N)-A-S–H gels with elevated Al/Si ratios.

Furthermore, no crystalline calcium carbonate and unreacted phases were detected, confirming the effectiveness of the synthesis and the sample preparation method applied in this study [48, 60]. This is particularly noteworthy, as earlier work reported difficulties in producing amorphous, Al-rich gels due to residual gibbsite and the formation of calcium carbonate phases [48].

The information on the d-spacing is limited, as no basal peaks are distinguished in the low-angle region between 5° and 10° [46]. According to Bragg's Law [61], an increase in d-spacing decreases the corresponding diffraction angle (2θ). If the d-spacing becomes sufficiently large, the associated 2θ value may fall below the detection limit of the XRD instrument (5° 2θ in this study), leading to undetectable

basal peaks. This suggests that the Al-rich C-(N)-A-S–H gels in this study possess high d-spacing, which explains the absence of observable basal reflections. Such high d-spacing can be attributed to several factors: a high content of bound water in the interlayer [61], substantial incorporation of Al into the gel structure, and a relatively low Ca content in the gel composition [46]. Although no sharp basal reflections are visible, the shift of the main amorphous hump (around 30°) toward lower 2θ values provides indirect evidence of an overall increase in average structural spacings [35]. Accordingly, a larger mean d-spacing can be assigned to the C0.5_A0.5 gel, as evidenced by its pronounced shift of the main amorphous bump to a lower 2θ value of 28.93°. This observation is consistent with the chemical composition of this gel.

Interestingly, the smallest d-spacing is observed in the C0.7_A0.5 gel, corresponding to the highest 2θ value of 29.47° for the amorphous bump, which is slightly higher 2θ than that of the C1.0_A0.3 gel (29.31°). Although C1.0_A0.3 contains a higher Ca/Si and lower Al/Si ratio, the reduced basal spacing in C0.7_A0.5 can be attributed to a greater substitution of Ca^{2+} by Na^{+} ions in the interlayer of gel [43]. This interpretation will be further discussed in Sect. 3.1.6.

3.1.2 Thermal analysis

Figure 4a and 4b display the thermal stability of the different gels through TGA and DTG curves, respectively. TGA curves show a total weight loss between 20.95 wt.% and 24.08 wt.% at the final temperature of 1000°C, while DTG curves identify the main thermal decomposition steps.

The initial thermal decomposition up to 200°C corresponds to the release of physically bound water (free water) [62]. Beyond this temperature, the mass loss gradually decreases with increasing temperature. As shown in Fig. 4a, the most pronounced weight loss peak occurs at around 120–130°C, due to the evaporation of physically bound water from the gel surfaces. A comparison among the gels further reveals that the C1.0_A0.3 gel contains the lowest free water content, consistent with its relatively high Ca/Si ratio, which promotes the formation of a denser structure [41].

The thermal decomposition between 250–300°C can indicate the presence of undissolved $Al(OH)_3$ [48]. As shown in Fig. 4a, the absence of intense peaks in this range suggests sufficient interaction among the reactants, confirming that the achieved Al/Si ratio in the solid phase accurately reflects the intended gel composition [48]. At higher temperatures, up to 400°C, chemically bound water is released from the gels [63], with the C1.0_A0.3 gel exhibiting a higher decomposition peak than the other gels.

Between approximately 500 and 800 °C, a minor weight loss is observed, attributed to calcium carbonate decomposition, most likely formed during the measurement process [64, 65]. This interpretation is

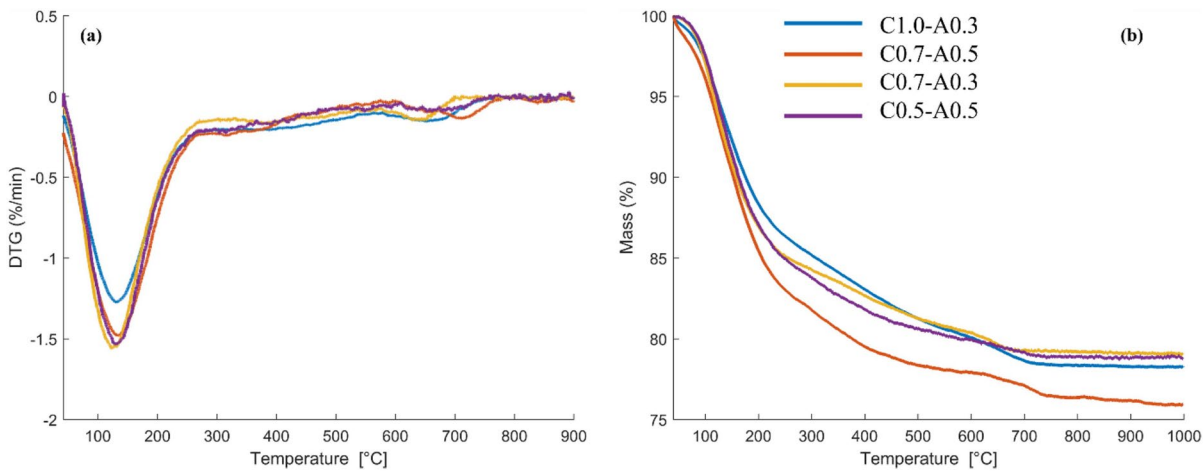

Fig. 4 Thermogravimetric curves of the synthetic gels with different molar ratios: (**a**) DTG curves and (**b**) TGA curves

supported by the XRD results (Fig. 3), which showed no crystalline calcium carbonate phases. However, other researchers have argued that the decomposition above 500°C may instead arise from residual nitrate within the structure of gels, which is undetectable by XRD [42].

The thermal decomposition behavior here is comparable to that of high aluminum C-A-S–H gels [42] and N-A-S–H gels [66], which also show free water loss at temperatures above 100°C. Since physically bound water in C-(N)-A-S–H-dominant gels is more easily released [21], typically at temperatures below 100°C [21, 67], this suggests that the synthetic gels in this study do not form a purely C-(N)-A-S–H structure.

As mentioned earlier, the C1.0_A0.3 gel shows a lower content of physically bound water and a slightly higher content of chemically bound water compared to the other gels (Fig. 4a). This observation may help clarify paste-level trends reported in the literature, where alkali-activated slag pastes contained less free water and more chemically bound water than slag/fly ash blends [68], reflecting differences in their predominant reaction products.

3.1.3 FTIR analysis

The FTIR spectra of the synthetic gels is presented in Fig. 5, with the corresponding band assignments detailed in Table 3. The dominant transmittance band, located between ~ 953 to 969 cm^{-1}, is assigned to the asymmetrical stretching vibrations of the Si–O–T bond, where T represents Si or Al in tetrahedral coordination [21, 47]. In addition, the bending vibrations

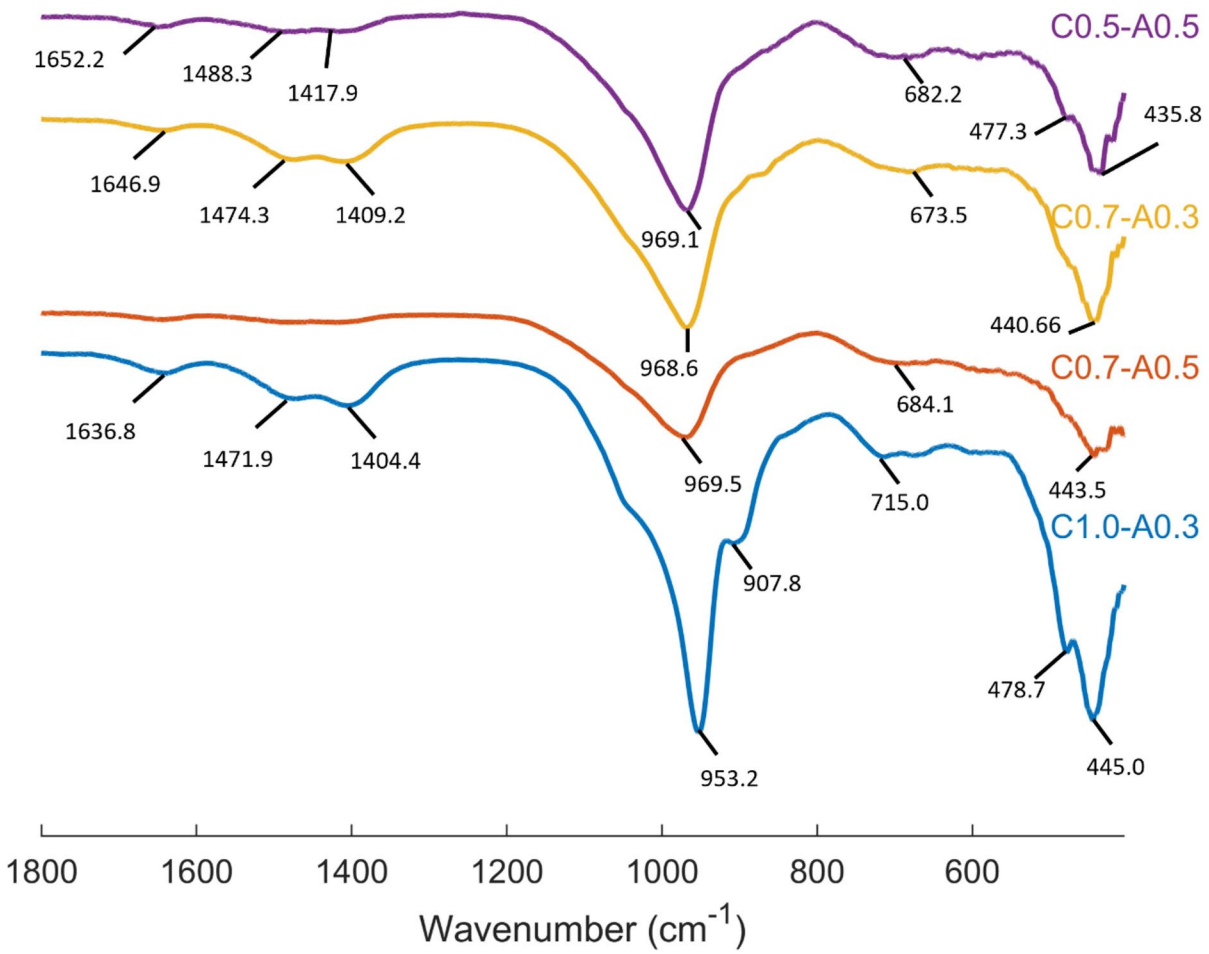

Fig. 5 Transmittance Infrared spectra of synthetic gels with different molar ratios

Table 3 Interpretation of the transmittance FTIR bands and their assignments [21, 42, 47, 69]

Bands	Wavenumbers (cm^{-1})				Band assignments
	C1.0_A0.3	C0.7_A0.5	C0.7_A0.3	C0.5_A0.5	
1	445.0	443.5	440.66	435.8	δ Si–O-Si/O-Si–O
2	478.7	–	–	477.3	δ Si–O-Si/O-Si–O
3	715.0	684.1	673.5	682.2	ν_s Si–O-Si, Al
4	907.8	–	–	–	ν_s Si–O-Si, Al
5	953.2	969.5	968.6	969.1	ν_{as} Si–O-Si, Al
6	1404.4	–	1409.2	1417.9	ν O-C-O
7	1471.9	–	1474.3	1488.3	ν O-C-O
8	1636.8	–	1646.9	1652.2	ν O–H

of Si–O–Si and O–Si–O bonds appear in the 435–478 cm^{-1} range. Except for the C0.7-A0.5 sample, minor carbonate bands are visible between 1400 and 1500 cm^{-1}, corresponding to the stretching vibrations of C-O bonds [21]. Similar carbonate features have been reported previously [42] and are attributed to the unavoidable interaction with atmospheric CO_2, consistent with the TGA analysis.

A systematic shift of the Si–O–T bonds to higher wavenumbers is observed as the Ca/Si ratio decreases below 1, accompanied by a reduction in band intensity. The broader and more curved band shapes in the C0.7_A0.5, C0.7_A0.3, and C0.5_A0.5 gels indicate a lower degree of crystallinity and a higher degree of polymerization compared to C1.0_A0.3 [69]. Among the studied gels, the highest wavenumbers for the Si–O–T bonds are observed in C0.7_A0.5 and C0.5_A0.5, attributed to their higher Al content, which promotes crosslinking and polymerization [1].

The band position for the Si–O–T bonds in all the studied gels is comparable to those reported for C-A-S–H [1, 42, 47] and typical C-(N)-A-S–H gels with $0.67 \leq Ca/(Al+Si) \leq 1.2$ [21, 46]. In contrast, comparison with literature shows less similarity to N–A–S–H/(N,C)-A-S–H gels, where the Si–O–T stretching vibrations are generally observed at higher wavenumbers, around 1000 cm^{-1}[7, 47, 48]. This finding is particularly notable given the low Ca/(Si + Al) ratios of the C0.7_A0.5, C0.7_A0.3, and C0.5_A0.5 gels in this study. Previous research has shown that in low-calcium systems where C-A-S–H and N-A-S–H coexist, reduced Ca content typically results in FTIR spectra resembling N-A-S–H or (N,C)-A-S–H gels [47]. Likewise, synthetic C-(N)-A-S–H/(N,C)-A-S–H gels with low Ca/Si ratios have been reported to display FTIR features more characteristic of N-A-S–H-type gels [21, 48]. One possible explanation for this discrepancy is the presence of crystalline Al-containing phases in those studies, as identified in their XRD patterns [21, 48]. The formation of secondary crystalline phases, such as zeolites, could contribute to spectral shifts and lead to an overestimation of stretching vibration frequencies. This interpretation is consistent with the findings of Chen et al. [35], who reported that the Si–O–T stretching vibrations in pure N-A-S–H gels occur at frequencies similar to those observed here, further supporting the amorphous nature of the gels analyzed in this study.

3.1.4 ^{29}Si NMR

Table 4 summarizes the chemical shift ranges, the corresponding structural environments and coordination states of the Q^n species as reported in the literature for AAMs. The Q^n notation describes distinct chemical environments of ^{29}Si atoms, where n denotes the number of oxygen atoms shared with neighboring tetrahedra in the Si–O network ($0 \leq n \leq 4$) [70, 71].

As can be seen in Table 4, three main regions can be distinguished for the reaction products: the C-(N)-A-S–H/C-A-S–H gel region (-78 to -87 ppm), typically associated with chain end (Q^1) and middle chain (Q^2) silicate tetrahedra; the (N,C)-A-S–H (hybrid) gel region (-88 to -92 ppm), as a combined $Q^3(1Al) + Q^4(4Al)$ contribution, reflecting overlapping signals from $Q^3(1Al)$ cross-linking sites in C-(N)-A-S–H/C-A-S–H gel and $Q^4(4Al)$ environments characteristic of N-A-S–H gels; and the N-A-S–H-like gel region (-86 to -125 ppm), which is dominated by three-dimensional framework structures

Table 4 Reacted/unreacted products, coordination states, and corresponding ^{29}Si NMR chemical shift ranges of Q^n species forming in AAMs

Products	Q^n Species	Structural coordination	Chemical shift range (ppm)	References
Unreacted monomers	Q^0	Isolated SiO_4	−70 ~ −78.5	[67]
C-(N)-A-S–H/C-A-S–H gel	Q^1	Chain end group tetrahedra	−78.5 ~ −80.50	[41]
	Q^2 (1Al)	Middle chain with one Al substitution	−80.5 ~ −83	[1, 26]
	Q^2	Middle chain tetrahedra (Q_p^2+Q_b^2 combined)	−84 ~ −87	[1, 2, 26]
(N,C)-A-S–H (hybrid) gel[a]	Q^3 (1Al) + Q^4 (4Al)	Combined contribution of Cross-linking Si with one Al neighbor and silicon tetrahedron with four Al neighbors	−88 ~ −92	[2, 26, 72, 78]
N-A-S–H-like environment[b]	Q^4 (3Al)	Silicon tetrahedron with three Al neighbors	−86 ~ −98.7	[2, 21, 75]
	Q^4 (2Al)	Silicon tetrahedron with two Al neighbors	−91 ~ −105	[2, 3, 21, 80]
	Q^4 (1Al)	Silicon tetrahedron with one Al neighbor	−97 ~ −109	[3, 21, 45]
	Q^4 (0Al)	Silica-rich networks	−104 ~ −125	[2, 67, 72]

[a] The −82 to −92 ppm region contains overlapping contributions from Q^3(1Al) (C-(N)-A-S–H crosslinking) and Q^4(4Al) (N-A-S–H gel) [26, 72] and can be attributed as the (N,C)-A-S–H gel [72]

[b] Q^4(mAl) signals can be interpreted as highly polymerized aluminosilicate environments (N-A-S–H-like), which may also include contributions from highly cross-linked C-(N)-A-S–H gel structures

primarily composed of Q^4(mAl) species (m = 0–4). It should be noted that while Q^4(0Al) sites are included in the N-A-S–H-like gel region in Table 4, resonances appearing at highly negative chemical shifts (< -112 ppm) are commonly attributed in the literature to unreacted precursor domains (e.g., unreactive fly ash or silica-rich glass). Similarly, Q^0 resonances in the −70 to −78.5 ppm range are generally associated with unreacted slag species in AAMs [65, 72]. To maintain methodological consistency with established approaches for distinguishing reaction products from unreacted phases in AAMs, spectral deconvolution of the synthesized gels in this study was carried out using the same criteria.

Figure 6 presents the ^{29}Si MAS NMR spectra of the synthetic gels with different molar ratios, together with the deconvoluted spectral contributions assigned to each Q^n species. A Gaussian function was employed for peak fitting and semi-quantitative deconvolution, as this lineshape adequately represents the broad distribution of chemical environments and is widely adopted in the literature [2, 19, 73, 74]. FWHM constraints were applied with an upper limit of 10 ppm during the deconvolution [65]. Specifically, narrower widths (≤5 ppm) were assigned to the C-(N)-A-S–H/C-A-S–H gel region [75], whereas broader values up to 10 ppm were allowed for the N-A-S–H-like sites [76, 77]. Moreover, for the overlapping Q^3(1Al) + Q^4(4Al) region ((N,C)-A-S–H), an intermediate constraint of FWHM ≤ 7 ppm was adopted [75]. Nevertheless, since ^{29}Si MAS NMR is sensitive only to short-range structural order, and because substantial spectral overlap exists among the Q^n(mAl) environments [78] particularly in the −88 to −92 ppm region, the deconvolution presented here is interpreted as representing variations in local silicon coordination environments rather than distinct spatially separated gel phases.

As shown in Fig. 6, two dominant regions can be identified in all spectra. The first region spans approximately −78.5 ± 0.5 ppm to −85 ± 0.5 ppm, which is mainly associated with the C-(N)-A-S–H or C-A-S–H-like gel structures. The second dominant region appears at −93 ± 1 ppm and extends toward more negative chemical shifts, corresponding to Q^4(mAl) environments, which is commonly associated with highly polymerized three-dimensional aluminosilicate frameworks (N-A-S–H-like gel) [65, 72].

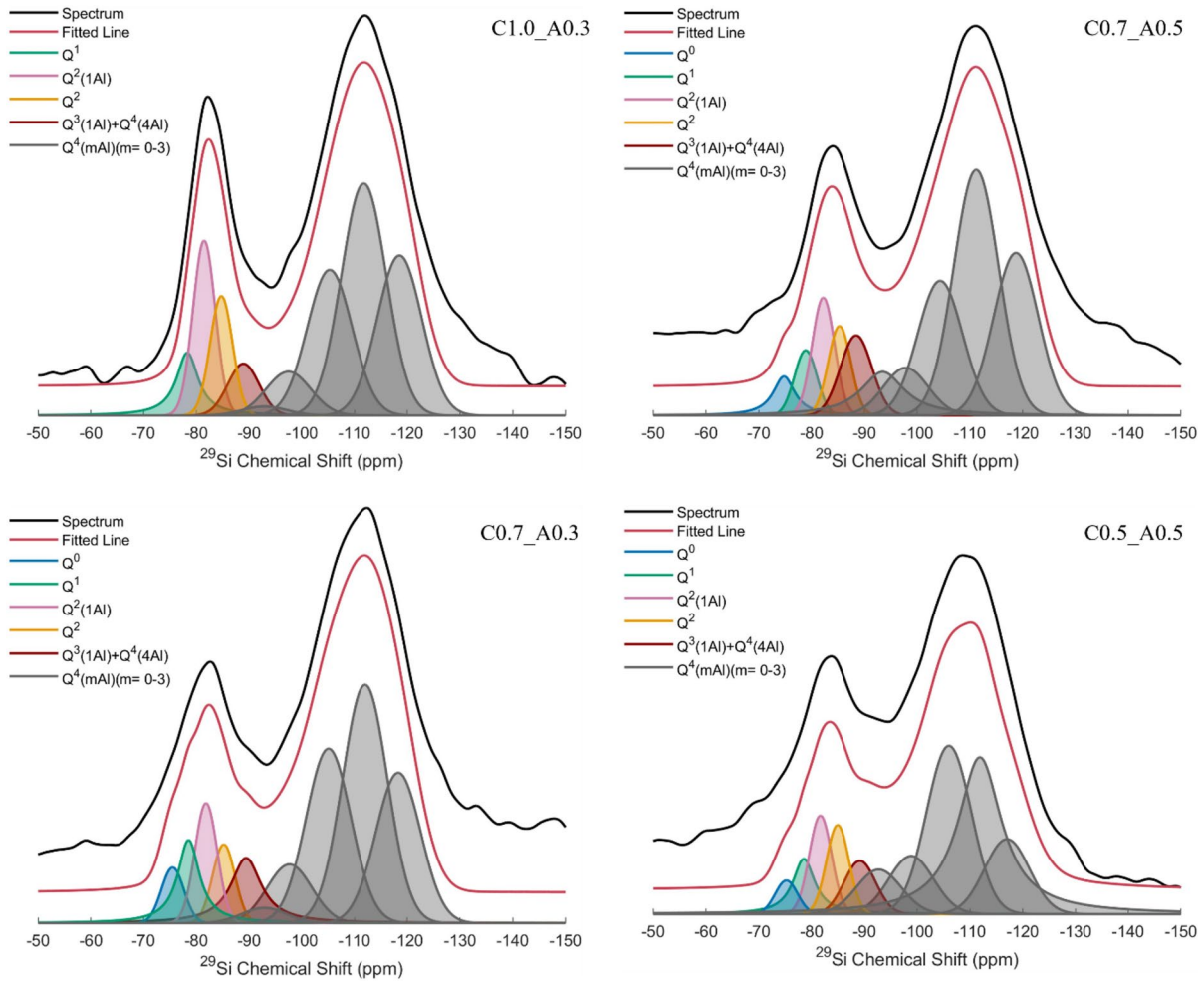

Fig. 6 ^{29}Si MAS NMR spectra of the synthetic gels with different molar ratios along with the deconvoluted areas

However, potential overlapping contributions from highly cross-linked C-(N)-A-S–H-like gels make clear distinction of these environments difficult. A more definitive distinction between chemically anhydrous N-A-S–H-type frameworks and proton-rich C-(N)-A-S–H environments could be achieved in future work using ^{1}H-^{29}Si CP-MAS NMR with variable contact-time experiments [75].

In addition to the dominant environments, a distinct resonance centered at -89 ± 0.5 ppm is observed in all spectra, consistent with the presence of the (N,C)-A-S–H hybrid gel environment. The relatively high proportion of Q^4(mAl)-type environments across all compositions reflects the prevalence of highly polymerized aluminosilicate domains within the synthesized gels. The coexistence of these local structural environments, comprising C-(N)-A-S–H/C-A-S–H, (N,C)-A-S–H, and N-A-S–H-like gels, is consistent with previous structural characterizations of AAMs [16, 21, 72]. Importantly, the assignment of the (N,C)-A-S–H environment at -89 ppm could be further strengthened in future work by heteronuclear ^{23}Na–^{29}Si correlation experiments [79], which would provide direct evidence of spatial proximity between sodium and silicon in this phase.

The semi-quantitative results obtained from spectral deconvolution are summarized in Table 5, and the full fitting parameters for each spectrum are reported in Table S1. As described previously, the identified environments are classified into the unreacted domains and reaction products. The unreacted fraction comprises Q^0 and Q^4(0Al) sites, while the

Table 5 Relative proportions (%) of the Q^n species obtained from ^{29}Si NMR spectral deconvolution of the synthetic gels, together with the average chemical shifts (δ_{Si}, ppm) and their observed variation

	Unreacted monomers	Local structural environments										Silica-rich network (unreacted precursor)
		C-A-S–H/C-(N)-A-S–H-like			(N,C)-A-S–H-like	N-A-S–H-like						
						Al-rich			Si-rich			
	Q^0	Q1	Q^2(1Al)	Q^2	Q^3 (1Al) + Q^4 (4Al)	Q^4 (3Al)	Q^4 (3Al)	Q^4 (2Al)	Q^4 (1Al)	Q^4 (0Al)		
	-75.16 ± 0.39 ppm	-78.56 ± 0.33 ppm	-81.80 ± 0.43 ppm	-85.05 ± 0.30 ppm	-88.99 ± 0.54 ppm	-93.00 ± 0.47 ppm	-97.96 ± 0.89 ppm	-105.19 ± 0.83 ppm	-111.71 ± 0.51 ppm	-118.14 ± 1.14 ppm		
C1.0_A0.3	0	5.66	10.65	7.28	4.43	1.12	5.36	17.75	28.25	19.50		
C0.7_A0.5	3.30	3.72	6.73	5.10	6.41	7.37	5.45	15.36	28	18.54		
C0.7_A0.3	3.12	6.87	6.72	4.41	7.55	1.72	6.59	19.52	26.66	16.84		
C0.5_A0.5	2.20	5.34	6.43	5.82	4.88	5.82	7.59	21.95	30.18	9.78		

reaction products include the gel-like environments. The persistence of the unreacted Si species indicates that the bulk Ca/Si and Al/Si ratios obtained from the XRF analysis (Table 2) should be regarded as nominal rather than effective compositional ratios, since a fraction of the Si is not incorporated into the gel-like reaction products. Consequently, the effective Ca/Si and Al/Si ratios within the reacted aluminosilicate network are expected to be slightly higher than the corresponding bulk molar ratios.

Within the Q^4-rich aluminosilicate environments, two compositional trends can be distinguished, corresponding to relatively Si-rich and Al-rich environments. The Si-rich type is primarily associated with Q^4(1Al) and Q^4(2Al) environments, whereas the Al-rich type is characterized by the proportion of Q^4(3Al) species. Two contributions assigned to Q^4(3Al) environments are identified at -93 ± 0.5 ppm and -98 ± 0.5 ppm, corresponding to more reactive highly polymerized aluminosilicate structures [72, 78].

According to the Table 5, the proportion of the C-A-S–H/C-(N)-A-S–H-like gel environments decrease progressively with decreasing Ca/Si ratio, from 23.6% in C1.0_A0.3 to about 15.6–18.0% in the AASB gels, consistent with the reduced availability of Ca^{2+} for C-A-S–H nucleation and growth. On the other hand, the total proportion of Q^4-rich aluminosilicate environments increases from about 52.5% in C1.0_A0.3 to between 56.2% and 65.5% in the gels with the lower Ca/Si ratio. The considerably higher proportion of Q^4-rich environments in C0.5_A0.5 might indicate that the combination of low Ca/Si (0.5) and high Al/Si (0.5) creates particularly favorable conditions for the formation of highly polymerized aluminosilicate domains. This is further supported by the observation that C0.5_A0.5 exhibits the lowest total amount of unreacted precursor with about 11.8% compared to 19.5–21.8% in other gels. The reduced unreacted Q^4(0Al) content suggests that low calcium availability along with higher Al content, rather than hindering reaction, promotes more complete dissolution.

Additionally, the highest fraction of Al-rich Q^4(3Al)-dominated environments can be observed in the C0.7_A0.5 and C0.5_A0.5 gels with the combined Q^4(3Al) contents of about 12.8% and 13.4% respectively. This increased fraction reflects enhanced aluminum incorporation the Q^4-rich aluminosilicate

network and a higher polymerization degree [19] when the bulk Al/Si ratio increases to 0.5. Furthermore, the higher fraction of the Al-rich structural environments reflects a greater replacement of Si–O–Si bonds with Si–O–Al linkages, which in turn contributes to enhanced mechanical performance, including higher compressive strength [80].

Moreover, the (N,C)-A-S–H hybrid environment accounts for approximately 4.4–7.6% of the total gel-like spectral contributions across all samples and the highest fractions are observed in C0.7_A0.3 (7.6%) and C0.7_A0.5 (6.4%), suggesting that the intermediate Ca/Si ratio of 0.7 favors more formation of this overlapping $Q^3(1Al)+Q^4(4Al)$ environment.

3.1.5 ^{27}Al NMR

Figure 7 presents the ^{27}Al NMR spectra of the synthetic gels. The chemical shifts associated with different aluminum coordination states are as follows: tetrahedral (Al(IV)) between 50 and 80 ppm, pentahedral (Al(V)) between 30 and 40 ppm, and octahedral (Al(VI)) between − 10 and 15 ppm [81]. A qualitative assessment was prioritized in this study, as the broad and asymmetric ^{27}Al resonances make quantitative deconvolution of the 1D spectra prone to systematic uncertainty, particularly without higher-dimensional NMR experiments, such as 3QMAS, to better resolve overlapping environments [19, 78].

In all gels, a dominant peak appears in the 59–68 ppm range, indicating the presence of tetrahedral Al and confirming its incorporation in the silica chain [82]. These Al(IV) peak positions vary systematically with Ca/Si ratio across the studied gels, shifting from ~ 60 ppm in the lower Ca/Si samples (C0.5_A0.5, C0.7_A0.3, and C0.7_A0.5) to ~ 67.4 ppm in C1.0_0.3. This trend is consistent with the findings of Yang et al. for synthesized C-(A)-S–H phases [79], who attributed these resonances to distinct bridging Al(IV) environments denoted $Al_d(IV)$ ($\delta iso = 61.8 \pm 0.4$ ppm) and $Al_c(IV)$ ($\delta iso = 67.4 \pm 0.3$ ppm), respectively. The two sites primarily differ in their interlayer charge-balancing species, with $Al_d(IV)$ associated with Ca^{2+} ions and $Al_c(IV)$ with $½Ca^{2+}$ and hydroxyl groups.

Low-intensity resonances corresponding to octahedral aluminum are also detected in the C0.7_A0.5 and C0.5_A0.5 gels. While narrow Al(VI)

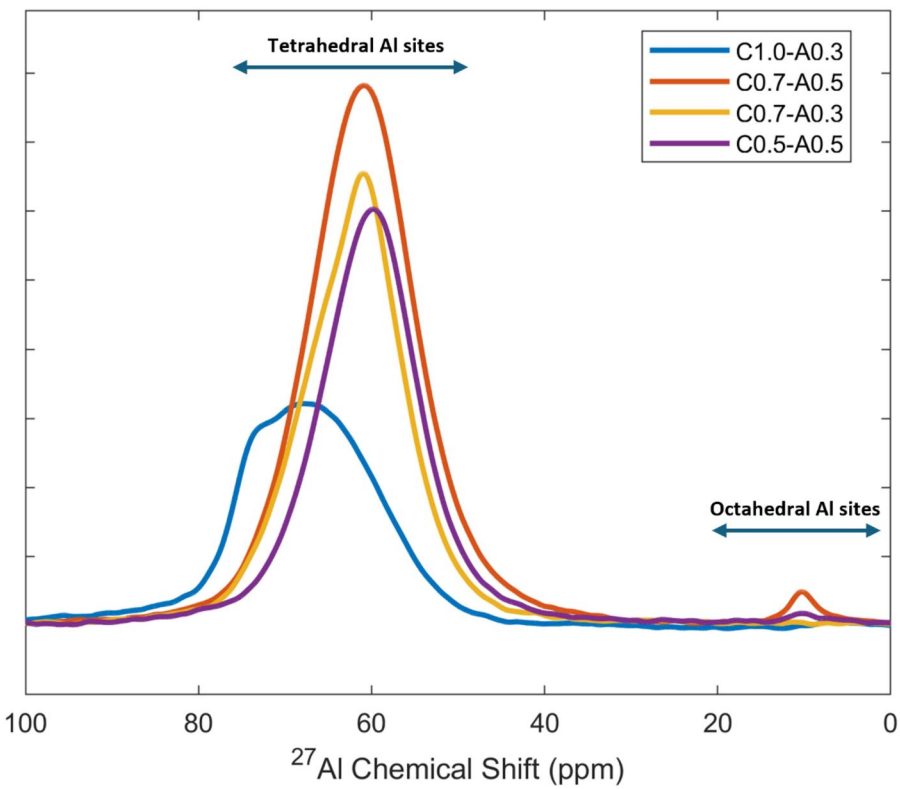

Fig. 7 ^{27}Al MAS NMR spectra of the synthetic gels with varying molar ratios

signals at approximately 5 ppm can represent bridging $[AlO_2(OH)_4]^{5-}$ network formers within the silicate chains of C-(A)-S–H gels, such species are predicted to be energetically unfavourable at Ca/Si < 1 [83]. Consequently, the weak Al(VI) signals observed in C0.7_A0.5 and C0.5_A0.5 more likely indicate saturation of tetrahedral sites [73], and an increased tendency toward highly polymerised N-A-S–H-like environments [45]. This finding is also consistent with previous research on C-(N)-A-S–H/N-A-S–H gel blends with Ca/(Si + Al) ratios > 0.67, which reported that increasing Al content favors the formation of Al-rich N-A-S–H phases when Ca remains constant [1, 2]. It is worth noting, however, the ^{27}Al NMR studies of calcium (sodium) aluminosilicate hydrate gels frequently reported the presence of secondary phases such as AFm phases, stratlingite, katoite, aluminum hydroxide, or hydrotalcite, depending on the specific system [1, 8, 78, 82], which can complicate the interpretation of Al(VI) coordination. In contrast, the absence of secondary phases in the present study substantially reduces the ambiguity associated with the assignment of Al(VI). Accordingly, the observed signal is more likely to reflect highly polymerized, N-A-S–H-like aluminosilicate environments, consistent with the ^{29}Si NMR observations.

Moreover, no detectable Al(V) resonances were observed between 30 and 40 ppm, indicating that penta-coordinated aluminum is not a stable component in these synthetic gels. This agrees with previous studies on alkali-activated slag and its blends, where Al(V) is either absent or only detected as a transient species in early-age reaction products [78, 84]. The lack of Al(V) suggests that aluminum in these gels primarily exists in well-defined tetrahedral and octahedral coordination states, consistent with the high degree of polymerization, as observed in ^{29}Si NMR.

3.1.6 ^{23}Na NMR

The ^{23}Na NMR spectra of synthetic gels are shown in Fig. 8. A single broad resonance is observed in all samples, ranging from -5.81 to -6.21 ppm. These chemical shifts are slightly lower than those typically reported for C-(N)-A-S–H gels (~-2 to -5 ppm) [1, 19, 46], but closer to the range reported for N-A-S–H gels (~-5 to -10.1 ppm) [44], suggesting a more constrained sodium environment.

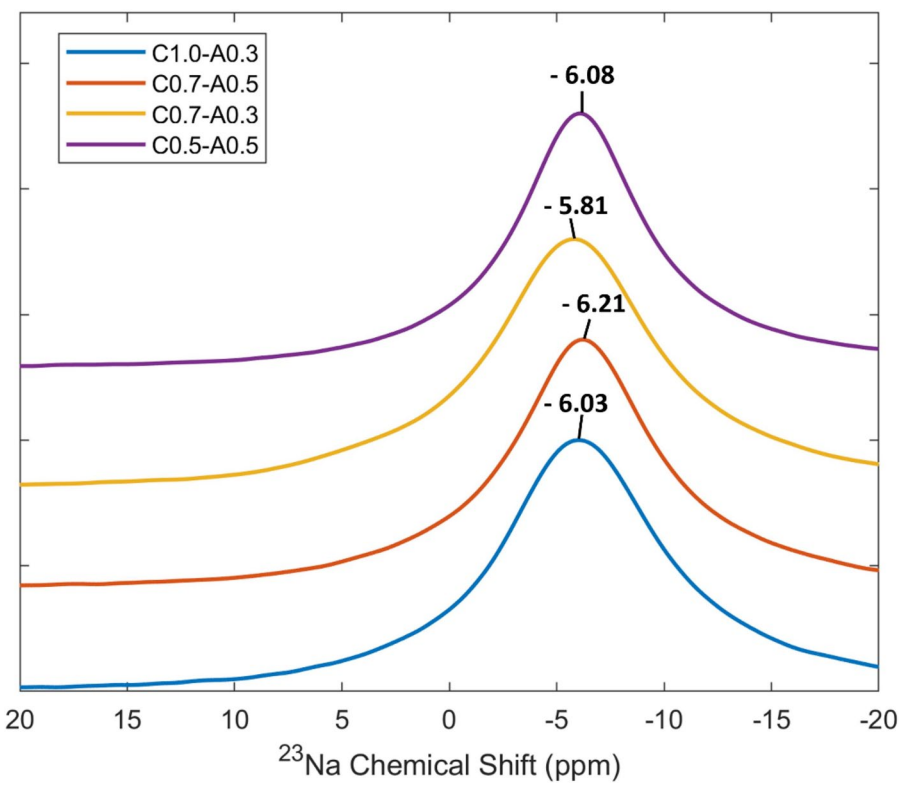

Fig. 8 ^{23}Na MAS NMR spectra of the synthetic gels with varying molar ratios; ^{23}Na NMR spectra are normalized to their respective maximum intensity to better compare peak positions

The region between -1 and -6 ppm generally corresponds to Na cations in a 5–6 coordinated environment [85]. However, the slightly more negative chemical shifts in some gels (Fig. 8) may indicate partial dehydration of sodium in a charge-balancing arrangement [86]. This partial dehydration likely results from the low relative humidity (RH) of the storage environment, which promotes the gradual removal of water molecules from the Na hydration shell [87]. As a result, the ^{23}Na NMR characteristics resemble those of N-A-S–H gels, where reduced "free water" availability produces a more rigid Na coordination environment [44]. Accordingly, since more positive ^{23}Na chemical shifts are generally associated with higher water molecules around Na^+[46, 86], the average hydration of Na^+ among the studied gels may follow the order: C0.7_A0.5 > C0.5_A0.5 > C1.0_A0.3 > C0.7_A0.3, based on the observed trend in Fig. 8.

In addition to the effects of dehydration, the variation in ^{23}Na chemical shift among the samples correlates with changes in the Na/Al molar ratio. As shown in Table 2, the Na/Al ratio in the Al-rich C-(N)-A-S–H gels ranges from 0.39 in C0.7_A0.5 to 1.95 in C0.7_A0.3. This increase is accompanied by a shift of the ^{23}Na NMR resonance, from -6.21 ppm in C0.7_A0.5 to -5.81 ppm in C0.7_A0.3. A similar trend was reported by Abdelrahman and Garg, who observed a shift in ^{23}Na chemical shift from –9.62 ppm to –4.93 ppm as the Na/Al ratio increased from 0.6 to 1.8 in N-A-S–H gels [88]. Their findings suggested that N-A-S–H gels with higher Na/Al ratios tend to be less polymerized, potentially more prone to leaching.

Overall, these findings suggest that both partial Na^+ dehydration and the Na/Al ratio strongly influence the local Na environment in Al-rich C-(N)-A-S–H gels, similar to trends previously observed in N-A-S–H gels.

3.2 Physical properties

Table 6 presents the BET results for synthetic gels. As observed, the average pore width falls between 0.82 and 1.14 nm, indicating the dominance of micropores (< 2 nm) within the gel structure.

The specific surface area of the synthetic gels varies significantly, from 67.33 ± 0.3501 to 198.85 ± 0.6160 m^2/g, values comparable to those reported for synthetic C-A-S–H gels [41, 89] and alkali-activated slag-blended pastes [90]. Among the samples, C1.0_A0.3 exhibits the lowest specific surface area (67.33 m^2/g) while also having the largest average particle size, which is attributed to its higher Ca/Si ratio [91]. By contrast, gels with lower Ca/Si ratios display higher specific surface areas and slightly smaller average particle sizes.

A direct comparison between C0.7_A0.3 and C0.7_A0.5 highlights the effect of increased Al uptake, which contributes to a higher specific surface area and a larger average particle size. A similar influence of Al on specific surface area has been previously reported for synthetic C-A-S–H gels [41, 89].

Interestingly, the physical properties of C0.5_A0.5 gel show similarities to those of C1.0_A0.3, despite their different chemical composition. The unexpectedly low specific surface area of C0.5_A0.5 gel may indicate pore collapse or dehydration-induced densification during the drying [68]. This behavior suggests that the C0.5_A0.5 gel is more susceptible to drying-induced structural alterations, likely due to its higher Al and lower Ca content.

4 Conclusions

This study provides a comprehensive evaluation of synthetic Al-rich C-(N)-A-S–H, a representative of

Table 6 The physical properties of gels with different molar ratios, obtained by BET

	Specific surface area (m^2/g)	Q_m (mmol/g)	R^2	Average particle size (nm)	Adsorption average pore width (nm)
C1.0_A0.3	67.33 ± 0.3501	0.69	0.9998	44.56	0.82
C0.7_A0.5	198.85 ± 0.6160	2.04	0.9999	30.17	1.14
C0.7_A0.3	148.08 ± 0.6980	1.52	0.9998	20.26	1.02
C0.5_A0.5	72.1605 ± 0.3785	0.74	0.9998	41.57	0.95

compositions commonly found in alkali-activated systems, including alkali-activated slag and slag-blended binders. By systematically varying the Ca/Si and Al/Si ratios, amorphous gels were successfully synthesized while preventing carbonation through controlled drying. The main findings are as follows:

(1) XRD analysis revealed a poorly crystalline C-S–H-like structure in all synthesized gels, independent of the composition. No crystalline secondary phases or calcium carbonates were detected, confirming the effectiveness of the synthesis and drying procedure in preserving phase purity.
(2) FTIR spectra exhibited Si–O–T asymmetric stretching bands at 953–969 cm^{-1}, consistent with C-(N)-A-S–H gels. Combined with TGA results, which indicated distinct water loss at higher temperatures, these findings support the coexistence of C-(N)-A-S–H and N-A-S–H-like phases across all studied compositions.
(3) ^{29}Si NMR deconvolution provided a semi-quantitative assessment of the distribution of local Q^n coordination environments, identifying contributions from C-(N)-A-S–H/C-A-S–H, (N,C)-A-S–H, and N-A-S–H-like aluminosilicate domains. The proportion of N-A-S–H-like environments increased from ~ 52.5% at Ca/Si = 1.0 to ~ 65.5% at lower Ca/Si ratios, indicating enhanced polymerization with decreasing Ca availability. Furthermore, the highest fractions of Al-rich $Q^4(3Al)$-type environments were observed in C0.7_A0.5 and C0.5_A0.5, suggesting increased Al incorporation into highly polymerized aluminosilicate frameworks at higher Al/Si ratios.
(4) ^{27}Al NMR confirmed Al predominantly in tetrahedral coordination across all gels. The systematic variation in Al(IV) chemical shift with Ca/Si ratio, transitioning from the $Al_d(IV)$ environment (~ 60 ppm) at low Ca/Si ratios to the $Al_c(IV)$ environment (~ 67.4 ppm) at higher Ca/Si ratios, reflects changes in the interlayer charge-balancing species. Octahedral Al, detected exclusively in gels with Al/Si = 0.5, providing direct evidence for N-A-S–H-like phase formation under high Al conditions in the absence of secondary phases.
(5) ^{23}Na NMR revealed chemical shifts ranging from − 5.81 to − 6.21 ppm across the gel series, closer to values reported for N-A-S–H-like gels than conventional C-(N)-A-S–H phases, confirming a more constrained Na coordination environment. The variation in chemical shifts correlated with both the Na/Al ratio and the degree of Na^+ hydration, with the average hydration of Na^+ following the order C0.7_A0.5 > C0.5_A0.5 > C1.0_A0.3 > C0.7_A0.3.
(6) BET analysis confirmed microporous structures with specific surface areas ranging from 67.33 to 198.85 m^2/g. Lower Ca/Si ratios and higher Al content generally increased surface area, whereas the anomalously low surface area of C0.5_A0.5 suggests pore collapse or dehydration-induced densification despite its high Al content.
(7) Multiple local gel environments were consistently identified across all investigated compositions without the formation of detectable crystalline phases. These findings suggest that, within the moderate Ca/Si compositional range studied here (0.50–1.04), high Al incorporation (Al/Si = 0.30–0.50) does not necessarily promote the formation of crystalline secondary phases when synthesis conditions are carefully controlled.

Acknowledgements The authors would like to thank the AshCycle project (Grant Agreement Number: 101058162) for the financial support throughout this work. We are especially grateful to Prof. John Provis and Dr. Swapna Ganapathy for their insightful guidance during the interpretation of ^{29}Si NMR spectra. We also thank Miss Katarina Rajić-Mišković from the Faculty of Applied Sciences at TU Delft for conducting the NMR analysis of the gel samples.

Funding European Commission,101058162,Guang Ye

Data Availability The datasets generated and analyzed during the current study are available from the corresponding author upon reasonable request. The raw data will be deposited in the TU Delft institutional repository following the completion of the first author's doctoral research, after which the data will be publicly accessible.

Appendix A

See Table 7 and 8.

Table 7 Characterisation of mixtures with the development of (C)-(N)-A-S–H gel in single systems

The studied application	Precursor (%100)	Activator	Gel type	Element content (wt%) and atomic ratios (obtained from EDS)								Ref
				Si	Ca	Na	Al	Ca/Si	Si/Al	Na/Si	Al/Si	
Alkali-activated paste	Slag	NaOH	C-(N)-A-S–H	0.58 ± 0.19	0.65 ± 0.14	4.33 ± 1.39	0.49 ± 0.17	1.12	1.18	0.58	0.84	[27]
		Na_2SiO_3 and NaOH		–	–	–	–	0.82 ± 0.04	2.96 ± 0.57	0.41 ± 0.14	0.34	[28]
		Na_2SiO_3 and NaOH		–	–	–	–	0.61–0.85	–	0.12–0.37	0.25–0.27	[29]
		Na_2SiO_3 and NaOH		–	–	–	–	1.03	–	–	0.45	[30]
		Na_2SiO_3 and NaOH		–	–	–	–	0.91–1.05	–	–	0.36–0.40	[31]
Alkali-activated concrete		Na_2SiO_3		–	–	–	–	1.1	–	0.21	0.29	[32]
Alkali-activated paste		NaOH		–	–	–	–	1.13–1.26	–	–	0.22–0.27	[33]
Alkali-activated paste		NaOH-4M + 10 g waste glass		–	–	–	–	1.33	2.1	–	0.48	[34]
Geopolymer paste	Basalt fiber	Na_2SiO_3 and NaOH	C-N-A-S–H	8.95	9.87	14.56	1.92	1.10	4.66	4.24	0.21	[92]
One-part geopolymer	Fly ash	Na_2SiO_3 and NaOH	(N)-(C)-A-S–H	–	–	–	–	0.27–0.68	–	–	0.42–0.69	[93]
Geopolymer composite		Na_2SiO_3 and NaOH	(C)-N-A-S–H	9.7	2.97	2.66	12.26	0.29	0.79	0.27	1.10	[94]

Table 8 Characterisation of mixtures with the development of (C)-(N)-A-S–H gel in blended systems

The studied application	Precursor	Activator	Gel type	Element content (wt%) and atomic ratios (obtained from EDS)										Ref
				Si	Ca	Na	Al	Ca/Si	Si/Al	Na/Si	Na/Al	Na/Ca	Al/Si	
Geopolymer concrete	15% OPC + 85% rice husk ash	Na_2SiO_3 and NaOH	C-N-A-S–H	23.33	27.12	18.13	2.31	1.16	10.10	0.78	7.84	0.67	0.099	[95]
Geopolymer paste	30% basalt fiber + 70% rice husk	Na_2SiO_3 and NaOH	C-N-A-S–H	11.88	9.54	9.35	5.44	0.80	2.18	0.79	1.72	0.98	0.45	[92]
	100% basalt fiber			8.95	9.87	14.56	1.92	1.10	4.66	1.63	7.58	1.48	0.21	
Alkali-activated pastes	Constant Fly ash and slag ratio: 0.8:0.2	Na_2SiO_3	C-N-A-S–H	–	–	–	–	0.37	2.52	0.27	0.65	–	0.40	[63]
		8% APC + 92% Na_2SiO_3		–	–	–	–	0.33	1.95	0.27	0.55	–	0.51	
		16% APC + 84% Na_2SiO_3		–	–	–	–	0.44	2.28	0.26	0.58	–	0.44	
		24% APC + 76% Na_2SiO_3		–	–	–	–	0.39	2.21	0.24	0.50	–	0.45	
Alkali-activated paste	Metakaolin and 20% limestone powder	Na_2SiO_3 and NaOH	Both N-A-S–H and N-(C)-A-S–H	–	–	–	–	0.05	1.97	0.38	0.74	–	0.51	[25]
	Metakaolin and 60% limestone powder			–	–	–	–	0.19	1.93	0.31	0.60	–	0.52	
Alkali-activated cements	50% fly ash and 50% slag	Na_2SiO_3 and NaOH	Both C-A-S–H and C-(N)-A-S–H	21.93	17.83	7.35	5.88	0.81	3.73	0.34	1.25	0.41	0.2–0.04	[96]
Alkali-activated binders and mortars	Fly ash /GGBS ratio = 80/20	Na_2SiO_3 and NaOH	Both N-A-S–H and C-A-S–H	12	4.3	–	5.3	0.4	2.3	–	–	–	0.44	[5]
	Fly ash /GGBS ratio = 30/70			10.3	6.5	–	3.3	0.6	3.1	–	–	–	0.32	
Geopolymer pastes	Fly ash/slag ratio = 80/20	Na_2SiO_3 and NaOH	C-A-S–H and/or C-(N)-A-S–H	–	–	–	–	0.59	–	–	–	–	0.32	[38]
	Fly ash/slag ratio = 60/40			–	–	–	–	0.77	–	–	–	–	0.37	
	Fly ash/slag ratio = 30/70			–	–	–	–	1.08	–	–	–	–	0.28	
Alkali-activated paste	Class F Flay ash/cement = 90/10	Na_2SiO_3 and NaOH	(C)-(N)-A-S–H	–	–	–	–	0.22–0.39	–	–	–	0.4–1.5	0.12 ± 0.04	[97]

The studied application	Precursor	Activator	Gel type	Element content (wt%) and atomic ratios (obtained from EDS)										Ref
				Si	Ca	Na	Al	Ca/Si	Si/Al	Na/Si	Na/Al	Na/Ca	Al/Si	
Alkali-activated paste	Fly ash/slag = 70/30 and	Na_2SiO_3 and NaOH	C-(N)-A-S–H	–	–	–	–	0.37	–	–	0.79	–	0.36	[30]
	Fly ash/slag = 30/70			–	–	–	–	0.85	–	–	1.82	–	0.31	
Geopolymer paste	GGBS/ sewage sludge ash = 50/50	Na_2SiO_3 and NaOH	C-(N)-A-S–H	–	–	–	–	0.32	2.16	0.23	–	–	–	[98]
Brick and concrete wastes geo-polymers	Concrete waste = 20 Red clay brick waste = 35 GGBS = 45	Na_2SiO_3 and NaOH	C-(N)-A-S–H and/or N-A-S–H	18.8	18.6	5.8	5.0	–	–	–	–	–	–	[99]
Alkali-activated paste	Constant Class F Fly ash and slag	Na_2SiO_3 and flue gas residues	C-N-A-S–H or both N-A-S–H and C-A-S–H	41	14.2	18	18.3	0.35	2.24	0.44	0.98	1.27	0.45	[39]
Alkali-activated paste	Waste glass/ GGBS = 75/25	Na_2SiO_3 and NaOH	C-(N)-A-S–H	–	–	–	–	0.34 ± 0.06	8.78 ± 3.02	0.27 ± 0.04	–	–	0.11	[28]
Alkali-activated mortars	Glass powder = 75 calcium aluminate cement = 10 GGBS = 15	Na_2SiO_3 and NaOH	C-(N)-A-S–H	19.25 ± 2.34	5.03 ± 0.68	6.19 ± 0.80	4.80 ± 0.55	0.26 ± 0.04	4.09 ± 0.86	0.32 ± 0.04			0.24	[100]
	Glass powder = 75 calcium aluminate cement = 15 GGBS = 10			23.75 ± 1.27	5.30 ± 0.36	7.89 ± 0.23	6.03 ± 0.29	0.22 ± 0.01	3.94 ± 0.25	0.33 ± 0.03			0.25	
Alkali-activated cellular concrete	80% MSWI bottom ash + 20% Waste glass powder	Waste glass powder acts as alkali activator	C-(N)-A-S–H	–	–	–	–	0.61	–	0.15	–	–	0.23	[101]
Alkali-activated binders	30% phosphate sludge + 30% kaolin clay + 30% glass waste	$NaOH + Na_2CO_3 + Na_2SO_4$	(N)-(C)-A-S–H and/or N-A-S–H	18.5 ± 0.92	9.67 ± 2.23	4.12 ± 0.42	7.09 ± 1.1	0.36 ± 0.07	2.67 ± 0.42	–	0.88 ± 0.13	–	0.37	[40]
				17.35 ± 1.07	7.34 ± 1.66	6.07 ± 0.78	7.22 ± 0.96	0.42 ± 0.1	2.46 ± 0.4	–	0.84 ± 0.07	–	0.41	

The studied application	Precursor	Activator	Gel type	Element content (wt%) and atomic ratios (obtained from EDS)										Ref
				Si	Ca	Na	Al	Ca/Si	Si/Al	Na/Si	Na/Al	Na/Ca	Al/Si	
Alkali-activated mortars	40%Glass powder + 30% GGBFS + 30% Fly ash	Na_2SiO_3 and NaOH	C-(N)-A-S–H	–	–	–	–	0.29	5.04	0.44	2.21	–	0.2	[102]
Alkali-activated mineral wools	67.4% stone wool + 32.6% NaOH and 59% stone wool + 41% $Na_2O.2SiO_2$	Na_2SiO_3 and NaOH	Both C-(N-)A-S–H and N-A-S–H	–	–	–	–	0.55–2.0	–	–	–	–	0.1	[23]
Alkali-activated pastes	50% fly ash + 50% GGBS	NaOH	C-(N)-A-S–H or C-A-S–H	–	–	–	–	1.02	1.98	–	–	–	0.51	[34]
	50% fly ash + 50% GGBS	NaOH activator + 10 g waste glass	C-N-A-S–H					1.41	2.01				0.50	
	50% fly ash + 50% GGBS	NaOH activator + 30 g waste glass	C-A-S–H or C-N-A-S–H					0.76	1.11				0.9	
			C-N-A-S–H					1.67	2.19				0.46	
alkali-activated Composites	76% fly ash + 19% GGBS + 5% silica fume	Anhydrous sodium metasilicate + waterglass	C-(N)-A-S–H	–	–	–	–	0.05–0.22	–	–	–	–	0.10–1.03	[103]
	47.5% fly ash + 47.5% GGBS + 5% silica fume			–	–	–	–	0.16–0.54	–	–	–	–	0.13–0.64	
	19% fly ash + 76% GGBS + 5% silica fume			–	–	–	–	0.33–0.70	–	–	–	–	0.15–0.39	
Alkali-activated pastes	30% slag + 70% fly ash	Na_2SiO_3 and NaOH	C-(N)-A-S–H	–	–	–	–	1.00 ± 0.16	–	–	–	–	0.35 ± 0.09	[104]
				–	–	–	–	0.39 ± 0.07	–	–	–	–	0.42 ± 0.06	
				–	–	–	–	0.33 ± 0.07	–	–	–	–	0.39 ± 0.06	
	50% slag + 50% fly ash			–	–	–	–	1.82 ± 0.53	–	–	–	–	0.34 ± 0.06	
				–	–	–	–	0.61 ± 0.03	–	–	–	–	0.42 ± 0.05	
				–	–	–	–	0.61 ± 0.04	–	–	–	–	0.40 ± 0.05	

The studied application	Precursor	Activator	Gel type	Element content (wt%) and atomic ratios (obtained from EDS)										Ref
				Si	Ca	Na	Al	Ca/Si	Si/Al	Na/Si	Na/Al	Na/Ca	Al/Si	
Alkali-activated binders	Fly ash / (fly ash + slag) = 0.75	Na_2SiO_3	C-N-A-S–H or both N-A-S–H and C-A-S–H	16.31	2.07	4.67	6.58	0.13	2.48	0.31	0.95	2.26	0.40	[105]
	Fly ash / (fly ash + slag) = 0.50			14.87	4.73	5.56	3.72	0.32	4	0.37	1.55	1.18	0.25	
	Fly ash / (fly ash + slag) = 0.25			14.57	5.80	4.31	2.95	0.40	4.94	0.29	1.49	0.74	0.20	
Alkali-Activated Binders	60%slag + 40% fly ash	Na_2SiO_3 and NaOH	(C)-N-A-S–H	–	–	–	–	1.1	2.9	–	–	–	0.34	[106]
Alkali–activated paste	15% Desulphurization dust + 85% slag	desulphurization dust acts as alkali activator	C-A-S–H and C-(N)-A-S–H	–	–	–	–	0.78–3.78	–	–	–	–	0–0.80	[24]
	15% Desulphurization dust + 85% slag + 5% addition of microsilica		C-(N)-A-S–H	–	–	–	–	0.45–2.52	–	–	–	–	0.08–0.42	
Alkali-activated paste	70% fly ash + 30% slag	Na_2SiO_3 and NaOH	C-(N)-A-S–H	10.73-28.34	1.87–9.01	4.82–10.77	2.01–9.23	0.11–0.32	1.17–12.96	0.23–1.22	–	–	–	[107]
Alkali activated binder	25% Electric arc furnace slag + 75% fly ash	Na_2SiO_3 and NaOH	Both N-A-S–H and C-A-S–H	11.02	2.05	5.55	3.16	0.19	3.49	0.50	1.76	2.71	0.29	[108]
Alkali-activated binder	Phosphogypsum + fly ash + slag	Na_2SiO_3 and NaOH	C-(N)-A-S–H	22.37	12.75	9.59	5.61	0.57	3.99	0.43	1.71	0.75	0.25	[109]
				18.49	11.22	6.57	5.44	0.61	3.40	0.36	1.21	0.59	0.29	
Alkali-activated paste	30%M300 + 70% slag	Na_2SiO_3 and NaOH	C-(N)-A-S–H	–	–	–	–	0.73	–	0.1	–	–	0.29	[110]
	30% MSWI bottom ash + 70% slag			–	–	–	–	0.77	–	0.39	–	–	0.33	

References

1. Walkley B, San Nicolas R, Sani MA et al (2016) Phase evolution of C-(N)-A-S-H/N-A-S-H gel blends investigated via alkali-activation of synthetic calcium aluminosilicate precursors. Cem Concr Res 89:120–135. https://doi.org/10.1016/j.cemconres.2016.08.010
2. Walkley B, Provis JL (2019) Solid-state nuclear magnetic resonance spectroscopy of cements. Materials Today Advances. 1(1):100007
3. Walkley B, San Nicolas R, Sani MA et al (2016) Phase evolution of Na_2O-Al_2O_3-SiO_2-H_2O gels in synthetic aluminosilicate binders. Dalton Trans 45:5521–5535. https://doi.org/10.1039/c5dt04878h
4. Awoyera P, Adesina A (2019) A critical review on application of alkali activated slag as a sustainable composite binder. Case Studies in Construction Materials 11:. https://doi.org/10.1016/j.cscm.2019.e00268
5. Rafeet A, Vinai R, Soutsos M, Sha W (2019) Effects of slag substitution on physical and mechanical properties of fly ash-based alkali activated binders (AABs). Cem Concr Res 122:118–135. https://doi.org/10.1016/j.cemconres.2019.05.003
6. Huang C, Wang Q, Zhao C et al (2023) Nanoscale insight into the effect of calcium on early-age polymerization of CNASH gels. J Phys Chem B 127:4338–4350. https://doi.org/10.1021/acs.jpcb.3c01953
7. Srinivasamurthy L, Chevali VS, Zhang Z et al (2022) Mechanical property and microstructure development in alkali activated fly ash slag blends due to efflorescence. Constr Build Mater 16(332):127273
8. Dai Z, Tran TT, Skibsted J (2014) Aluminum incorporation in the C-S-H phase of white portland cement-metakaolin blends studied by ^{27}Al and ^{29}Si MAS NMR spectroscopy. J Am Ceram Soc 97:2662–2671. https://doi.org/10.1111/jace.13006
9. Shah IH, Miller SA, Jiang D, Myers RJ (2022) Cement substitution with secondary materials can reduce annual global CO2 emissions by up to 1.3 gigatons. Nat Commun 13:. https://doi.org/10.1038/s41467-022-33289-7
10. Huang G, Ji Y, Li J et al (2018) Use of slaked lime and Portland cement to improve the resistance of MSWI bottom ash-GBFS geopolymer concrete against carbonation. Constr Build Mater 166:290–300. https://doi.org/10.1016/j.conbuildmat.2018.01.089
11. Chen B, Perumal P, Illikainen M, Ye G (2023) A review on the utilization of municipal solid waste incineration (MSWI) bottom ash as a mineral resource for construction materials. J Build Eng. https://doi.org/10.1016/j.jobe.2023.106386
12. Chen B, Perumal P, Aghabeyk F et al (2024) Advances in using municipal solid waste incineration (MSWI) bottom ash as precursor for alkali-activated materials: A critical review. Resour Conserv Recycl 1(204):107516
13. Lei Z, Pavia S, Wang X (2024) Biomass ash waste from agricultural residues: Characterisation, reactivity and potential to develop one-part geopolymer cement. Constr Build Mater 14(431):136544
14. Samson G, Cyr M, Gao XX (2017) Formulation and characterization of blended alkali-activated materials based on flash-calcined metakaolin, fly ash and GGBS. Constr Build Mater 144:50–64. https://doi.org/10.1016/j.conbuildmat.2017.03.160
15. Li J, Yi C, Chen Z et al (2022) Relationships between reaction products and carbonation performance of alkali-activated slag with similar pore structure. Journal of Building Engineering. 1(45):103605
16. Zhang DW, Yang TT, Xu XG et al (2024) Relationship between MO/(SiO2+ Al2O3) of materials—amorphous gel structure—properties of the one-part FA-Slag-based AAMs. J Environ Chem Eng 12(6):114519
17. Barzgar S, Yan Y, Tarik M et al (2022) A long-term study on structural changes in calcium aluminate silicate hydrates. Mater Struct. https://doi.org/10.1617/s11527-022-02080-x
18. Bae SJ, Park S, Lee HK (2020) Role of Al in the crystal growth of alkali-activated fly ash and slag under a hydrothermal condition. Constr Build Mater 10(239):117842
19. Walkley B, Page SJ, Rees GJ et al (2020) Nanostructure of CaO-(Na_2O)-Al_2O_3-SiO_2-H_2O gels revealed by multinuclear solid-state magic angle spinning and multiple quantum magic angle spinning nuclear magnetic resonance spectroscopy. J Phys Chem C 124:1681–1694. https://doi.org/10.1021/acs.jpcc.9b10133
20. Garcia-Lodeiro I, Palomo A, Fernández-Jiménez A (2015) An overview of the chemistry of alkali-activated cement-based binders. Handbook of alkali-activated cements, mortars and concretes. Elsevier Inc., pp 19–47. https://doi.org/10.1533/9781782422884.1.19
21. Wang Y, Cao Y, Zhang Z et al (2023) Intrinsic sulfuric acid resistance of C-(N)-ASH and NASH gels produced by alkali-activation of synthetic calcium aluminosilicate precursors. Cem Concr Res 1(165):107068
22. Krivenko P (2017) Why alkaline activation - 60 years of the theory and practice of alkali-activated materials. J Ceram Sci Technol 8:323–333. https://doi.org/10.4416/JCST2017-00042
23. Yliniemi J, Walkley B, Provis JL et al (2020) Nanostructural evolution of alkali-activated mineral wools. Cem Concr Compos 106:103472
24. Adesanya E, Ohenoja K, Di Maria A et al (2020) Alternative alkali-activator from steel-making waste for one-part alkali-activated slag. J Clean Prod 274:123020
25. Perez-Cortes P, Escalante-Garcia JI (2020) Gel composition and molecular structure of alkali-activated metakaolin-limestone cements. Cem Concr Res 137:106211
26. Myers RJ, Bernal SA, San Nicolas R, Provis JL (2013) Generalized structural description of calcium-sodium aluminosilicate hydrate gels: the cross-linked substituted tobermorite model. Langmuir 29:5294–5306. https://doi.org/10.1021/la4000473
27. De Filippis U, Prud'Homme E, Meille S (2021) Relation between activator ratio, hydration products and mechanical properties of alkali-activated slag. Constr Build Mater 10(266):120940
28. Ali HA, Sun K, Xuan D et al (2023) Recycling of high-volume waste glass powder in alkali-activated materials: an efflorescence mitigation strategy. J Build Eng 65:105756
29. Nedeljković M, Ghiassi B, Ye G (2021) Role of curing conditions and precursor on the microstructure and phase

chemistry of alkali-activated fly ash and slag pastes. Materials (Basel). https://doi.org/10.3390/ma14081918
30. Zhang W, Yao X, Yang T, Zhang Z (2018) The degradation mechanisms of alkali-activated fly ash/slag blend cements exposed to sulphuric acid. Constr Build Mater 186:1177–1187. https://doi.org/10.1016/j.conbuildmat.2018.08.050
31. Lu C, Zhang Z, Hu J et al (2022) Relationship between rheological property and early age-microstructure building up of alkali-activated slag. Compos B Eng 247:110271
32. San Nicolas R, Bernal SA, Mejía De Gutiérrez R et al (2014) Distinctive microstructural features of aged sodium silicate-activated slag concretes. Cem Concr Res 65:41–51. https://doi.org/10.1016/j.cemconres.2014.07.008
33. Zuo Y, Nedeljković M, Ye G (2018) Coupled thermodynamic modelling and experimental study of sodium hydroxide activated slag. Constr Build Mater 188:262–279. https://doi.org/10.1016/j.conbuildmat.2018.08.087
34. Sasui S, Kim G, Nam J et al (2020) Incorporation of waste glass as an activator in Class-C Fly Ash/GGBS based Alkali activated material. Materials 13(17):3906
35. Chen Y, de Lima LM, Li Z et al (2024) Synthesis, solubility and thermodynamic properties of N-A-S-H gels with various target Si/Al ratios. Cem Concr Res. https://doi.org/10.1016/j.cemconres.2024.107484
36. Guan X, Jiang L, Fan D et al (2022) Molecular simulations of the structure-property relationships of NASH gels. Constr Build Mater 25(329):127166
37. Bernal SA, Provis JL (2014) Durability of alkali-activated materials: progress and perspectives. J Am Ceram Soc 97:997–1008. https://doi.org/10.1111/jace.12831
38. Aiken TA, Kwasny J, Sha W, Soutsos MN (2018) Effect of slag content and activator dosage on the resistance of fly ash geopolymer binders to sulfuric acid attack. Cem Concr Res 111:23–40. https://doi.org/10.1016/j.cemconres.2018.06.011
39. Riaz Ahmad M, Khan M, Wang A et al (2023) Alkali-activated materials partially activated using flue gas residues: an insight into reaction products. Constr Build Mater 371:130760
40. Moukannaa S, Aboulayt A, Hakkou R et al (2022) Fusion of phosphate by-products and glass waste for preparation of alkali-activated binders. Compos B Eng 1(242):110044
41. Zhang X, Wang B, Chang J (2024) Adsorption behavior and solidification mechanism of Pb (II) on synthetic CASH gels with different Ca/Si and Al/Si ratios in high alkaline conditions. Chem Eng J 1(493):152344
42. Kapeluszna E, Kotwica Ł, Różycka A, Gołek Ł (2017) Incorporation of Al in C-A-S-H gels with various Ca/Si and Al/Si ratio: microstructural and structural characteristics with DTA/TG, XRD, FTIR and TEM analysis. Constr Build Mater 155:643–653. https://doi.org/10.1016/j.conbuildmat.2017.08.091
43. L'Hôpital E, Lothenbach B, Scrivener K, Kulik DA (2016) Alkali uptake in calcium alumina silicate hydrate (C-A-S-H). Cem Concr Res 85:122–136. https://doi.org/10.1016/j.cemconres.2016.03.009
44. Shamo E, Charpentier T, Moskura M et al (2024) Synthesis methodology of pure N–A–S–H gels with wide range of Si/Al ratios at ambient temperature. J Am Ceram Soc 107:7537–7549. https://doi.org/10.1111/jace.20012
45. Mills J, Mondal P, Wagner N (2022) Structure-property relationships and state behavior of alkali-activated aluminosilicate gels. Cem Concr Res 1(151):106618
46. Liu C, Li Z, Nie S et al (2024) Structural evolution of calcium sodium aluminosilicate hydrate (C-(N-) ASH) gels induced by water exposure: the impact of Na leaching. Cem Concr Res 1(178):107432
47. Garcia-Lodeiro I, Palomo A, Fernández-Jiménez A, MacPhee DE (2011) Compatibility studies between N-A-S-H and C-A-S-H gels. Study in the ternary diagram Na_2O-CaO-Al_2O_3-SiO_2–H_2O. Cem Concr Res 41:923–931. https://doi.org/10.1016/j.cemconres.2011.05.006
48. Ye H, Huang L (2020) Degradation mechanisms of alkali-activated binders in sulfuric acid: The role of calcium and aluminum availability. Constr Build Mater 20(246):118477
49. Nedeljković M, Ghiassi B, van der Laan S et al (2019) Effect of curing conditions on the pore solution and carbonation resistance of alkali-activated fly ash and slag pastes. Cem Concr Res 116:146–158. https://doi.org/10.1016/j.cemconres.2018.11.011
50. Sinha A, Wei J (2024) Phase, structure, and hygroscopic property evolutions of alkali-silica reaction gels under freeze drying. Cem Concr Res 1(186):107692
51. Liu X, Feng P, Yu X et al (2022) The physiochemical alterations of calcium silicate hydrate (CSH) under magnesium attack. Cem Concr Res 1(160):106901
52. Ping Y, Kirkpatrick RJ, Brent P et al (1999) Structure of calcium silicate hydrate (C-S-H): near-, mid-, and far-infrared spectroscopy. J Am Ceram Soc 82:742–748. https://doi.org/10.1111/j.1151-2916.1999.tb01826.x
53. Ben Haha M, Le Saout G, Winnefeld F, Lothenbach B (2011) Influence of activator type on hydration kinetics, hydrate assemblage and microstructural development of alkali activated blast-furnace slags. Cem Concr Res 41:301–310. https://doi.org/10.1016/j.cemconres.2010.11.016
54. Krüger ME, Heisig A, Hilbig H et al (2023) Effect of aluminum on the structure of synthetic alkali-silica gels. Cem Concr Res. https://doi.org/10.1016/j.cemconres.2022.107088
55. Chi M, Huang R (2013) Binding mechanism and properties of alkali-activated fly ash/slag mortars. Constr Build Mater 40:291–298. https://doi.org/10.1016/j.conbuildmat.2012.11.003
56. Chen W, Li B, Wang J, Thom N (2021) Effects of alkali dosage and silicate modulus on autogenous shrinkage of alkali-activated slag cement paste. Cem Concr Res 1(141):106322
57. Hamdan A, Song H, Yao Z et al (2023) Modifications to reaction mechanisms, phase assemblages and mechanical properties of alkali-activated slags induced by gypsum addition. Cem Concr Res. https://doi.org/10.1016/j.cemconres.2023.107311
58. Kamath M, Prashant S, Kumar M (2021) Micro-characterisation of alkali activated paste with fly ash-GGBS-metakaolin binder system with ambient setting characteristics. Constr Build Mater 29(277):122323
59. Sun R, Fang C, Zhang H et al (2021) Chemo-mechanical properties of alkali-activated slag/fly ash paste incorporating white mud. Constr Build Mater 12(291):123312

60. Liu X, Feng P, Cai Y et al (2022) Carbonation behaviors of calcium silicate hydrate (CSH): effects of aluminum. Constr Build Mater 28(325):126825
61. Ma Y, Li W, Jin M et al (2022) Influences of leaching on the composition, structure and morphology of calcium silicate hydrate (C–S–H) with different Ca/Si ratios. J. Build. Eng. 15(58):105017
62. Sun X, Liu J, Qiu J et al (2022) Alkali activation of blast furnace slag using a carbonate-calcium carbide residue alkaline mixture to prepare cemented paste backfill. Constr Build Mater 21(320):126234
63. Ahmad MR, Qian LP, Fang Y et al (2023) A multiscale study on gel composition of hybrid alkali-activated materials partially utilizing air pollution control residue as an activator. Cem Concr Compos 136:104856
64. Maddalena R, Li K, Chater PA et al (2019) Direct synthesis of a solid calcium-silicate-hydrate (C-S-H). Constr Build Mater 223:554–565. https://doi.org/10.1016/j.conbuildmat.2019.06.024
65. Bernal SA, Provis JL, Walkley B et al (2013) Gel nanostructure in alkali-activated binders based on slag and fly ash, and effects of accelerated carbonation. Cem Concr Res 53:127–144. https://doi.org/10.1016/j.cemconres.2013.06.007
66. Rosas-Casarez CA, Arredondo-Rea SP, Gómez-Soberón JM et al (2014) Experimental study of XRD, FTIR and TGA techniques in geopolymeric materials. Int J Adv Comput Sci Appl 4(4):221–226
67. Wang Y, Cao Y, Zhang Z et al (2022) Study of acidic degradation of alkali-activated materials using synthetic C-(N)-ASH and NASH gels. Compos B Eng 1(230):109510
68. Ismail I, Bernal SA, Provis JL et al (2013) Drying-induced changes in the structure of alkali-activated pastes. J Mater Sci 48:3566–3577. https://doi.org/10.1007/s10853-013-7152-9
69. Yusuf MO (2023) Bond Characterization in Cementitious Material Binders Using Fourier-Transform Infrared Spectroscopy. Appl Sci 13(5):3353
70. Ouyang X, Wang L, Xu S et al (2020) Surface characterization of carbonated recycled concrete fines and its effect on the rheology, hydration and strength development of cement paste. Cem Concr Compos 114:103809. https://doi.org/10.1016/j.cemconcomp.2020.103809
71. Ma Y, Jin M, Li W et al (2024) Effect of drying method on calcium silicate hydrate (CSH): experiments and molecular dynamics simulations study. Constr Build Mater 12(411):134367
72. Fang G, Zhang M (2020) Multiscale micromechanical analysis of alkali-activated fly ash-slag paste. Cem Concr Res 135:106141. https://doi.org/10.1016/j.cemconres.2020.106141
73. Mills JN, Wagner NJ, Mondal P (2021) Relating chemical composition, structure, and rheology in alkali-activated aluminosilicate gels. J Am Ceram Soc 104:572–583. https://doi.org/10.1111/jace.17459
74. Walkley B, Ke X, Hussein OH et al (2020) Incorporation of strontium and calcium in geopolymer gels. J Hazard Mater. https://doi.org/10.1016/j.jhazmat.2019.121015
75. Walkley B, Ke X, Provis JL, Bernal SA (2021) Activator anion influences the nanostructure of alkali-activated slag cements. J Phys Chem C 125:20727–20739. https://doi.org/10.1021/acs.jpcc.1c07328
76. Walkley B, Ke X, Hussein O, Provis JL (2021) Thermodynamic properties of sodium aluminosilicate hydrate (N-A-S-H). Dalton Trans 50:13968–13984. https://doi.org/10.1039/d1dt02202d
77. Gevaudan JP, Wallat JD, Lama B, Srubar WV (2020) PVA- and PEG-assisted sol-gel synthesis of aluminosilicate precursors for N-A-S-H geopolymer cements. J Am Ceram Soc 103:859–877. https://doi.org/10.1111/jace.16764
78. Gao X, Yu QL, Brouwers HJH (2017) Apply 29Si, 27Al MAS NMR and selective dissolution in identifying the reaction degree of alkali activated slag-fly ash composites. Ceram Int 43:12408–12419. https://doi.org/10.1016/j.ceramint.2017.06.108
79. Yang SY, Yan Y, Lothenbach B, Skibsted J (2021) Incorporation of sodium and aluminum in cementitious calcium-alumino-silicate-hydrate C-(A)-S-H phases studied by ^{23}Na, ^{27}Al, and ^{29}Si MAS NMR spectroscopy. J Phys Chem C 125:27975–27995. https://doi.org/10.1021/acs.jpcc.1c08419
80. M S, R J, P RN (2021) Effect of change in the silica modulus of sodium silicate solution on the microstructure of fly ash geopolymers. J Build Eng. https://doi.org/10.1016/j.jobe.2021.102939
81. Lee NK, Koh KT, An GH, Ryu GS (2017) Influence of binder composition on the gel structure in alkali activated fly ash/slag pastes exposed to elevated temperatures. Ceram Int 43:2471–2480. https://doi.org/10.1016/j.ceramint.2016.11.042
82. L'Hôpital E, Lothenbach B, Le Saout G et al (2015) Incorporation of aluminium in calcium-silicate-hydrates. Cem Concr Res 75:91–103. https://doi.org/10.1016/j.cemconres.2015.04.007
83. Kunhi Mohamed A, Moutzouri P, Berruyer P et al (2020) The atomic-level structure of cementitious calcium aluminate silicate hydrate. J Am Chem Soc 142:11060–11071. https://doi.org/10.1021/jacs.0c02988
84. Fernández-Jiménez A, Puertas F, Sobrados I, Sanz J (2003) Structure of calcium silicate hydrates formed in alkaline-activated slag: influence of the type of alkaline activator. J Am Ceram Soc 86:1389–1394. https://doi.org/10.1111/j.1151-2916.2003.tb03481.x
85. Srinivasamurthy L, Chevali VS, Zhang Z, Wang H (2023) Effect of fly ash to slag ratio and Na2O content on leaching behaviour of fly Ash/Slag based alkali activated materials. Constr Build Mater 20(383):131234
86. Fernández-Jiménez A, Palomo, A. (2009). Nanostructure/microstructure of fly ash geopolymers. Geopolymers (pp. 89–117). https://doi.org/10.1533/9781845696382.1.89
87. Yang SY, Skibsted J (2024) Sodium sites and hydration state in C-S-H phases synthesized under alkaline conditions from 1H and 23Na NMR experiments. J Phys Chem C 128:10888–10902. https://doi.org/10.1021/acs.jpcc.4c01982
88. Abdelrahman O, Garg N (2022) Impact of Na/Al ratio on the extent of alkali-activation reaction: non-linearity and diminishing returns. Front Chem. https://doi.org/10.3389/fchem.2021.806532

89. Cai W, Xu Z, Zhang Z et al (2022) Chloride binding behavior of synthesized reaction products in alkali-activated slag. Compos B Eng 1(238):109919
90. Babaee M, Castel A (2018) Water vapor sorption isotherms, pore structure, and moisture transport characteristics of alkali-activated and Portland cement-based binders. Cem Concr Res 113:99–120. https://doi.org/10.1016/j.cemconres.2018.07.006
91. Wang J, Hu Z, Chen Y et al (2022) Effect of Ca/Si and Al/Si on micromechanical properties of C (-A)-SH. Cem Concr Res 1(157):106811
92. Saloni P, Pham TM (2020) Enhanced properties of high-silica rice husk ash-based geopolymer paste by incorporating basalt fibers. Constr Build Mater 245:118422. https://doi.org/10.1016/j.conbuildmat.2020.118422
93. Wan-En O, Yun-Ming L, Cheng-Yong H et al (2022) Towards greener one-part geopolymers through solid sodium activators modification. J Clean Prod 378:134370. https://doi.org/10.1016/j.jclepro.2022.134370
94. Qu F, Li W, Wang K et al (2021) Performance deterioration of fly ash/slag-based geopolymer composites subjected to coupled cyclic preloading and sulfuric acid attack. J Clean Prod 321:128942. https://doi.org/10.1016/j.jclepro.2021.128942
95. Saloni P, Yan Lim Y, Pham TM (2021) Influence of Portland cement on performance of fine rice husk ash geopolymer concrete: Strength and permeability properties. Constr Build Mater 300:124321. https://doi.org/10.1016/j.conbuildmat.2021.124321
96. Pinheiro C, Rios S, Viana da Fonseca A et al (2020) Application of the response surface method to optimize alkali activated cements based on low-reactivity ladle furnace slag. Constr Build Mater 264:120271. https://doi.org/10.1016/j.conbuildmat.2020.120271
97. Kaja AM, Lazaro A, Yu QL (2018) Effects of Portland cement on activation mechanism of class F fly ash geopolymer cured under ambient conditions. Constr Build Mater 189:1113–1123. https://doi.org/10.1016/j.conbuildmat.2018.09.065
98. Chen Z, Li JS, Zhan BJ et al (2018) Compressive strength and microstructural properties of dry-mixed geopolymer pastes synthesized from GGBS and sewage sludge ash. Constr Build Mater 182:597–607. https://doi.org/10.1016/j.conbuildmat.2018.06.159
99. Mahmoodi O, Siad H, Lachemi M, Sahmaran M (2021) Synthesis and optimization of binary systems of brick and concrete wastes geopolymers at ambient environment. Constr Build Mater 276:122217. https://doi.org/10.1016/j.conbuildmat.2020.122217
100. Ali HA, Xuan D, Lu JX, Poon CS (2022) Enhancing the resistance to microbial induced corrosion of alkali-activated glass powder/GGBS mortars by calcium aluminate cement. Constr Build Mater 341:127912. https://doi.org/10.1016/j.conbuildmat.2022.127912
101. Xuan D, Tang P, Poon CS (2019) MSWIBA-based cellular alkali-activated concrete incorporating waste glass powder. Cem Concr Compos 95:128–136. https://doi.org/10.1016/j.cemconcomp.2018.10.018
102. Khan MNN, Kuri JC, Sarker PK (2021) Effect of waste glass powder as a partial precursor in ambient cured alkali activated fly ash and fly ash-GGBFS mortars. J Build Eng 34:101934. https://doi.org/10.1016/j.jobe.2020.101934
103. Lao JC, Huang BT, Fang Y et al (2023) Strain-hardening alkali-activated fly ash/slag composites with ultra-high compressive strength and ultra-high tensile ductility. Cem Concr Res 165:107075. https://doi.org/10.1016/j.cemconres.2022.107075
104. Zhang S (2022) Micromechanics-guided development of strain- hardening alkali-activated composites Towards a low-carbon built environment
105. Marjanović N, Komljenović M, Baščarević Z, Nikolić V (2015) Comparison of two alkali-activated systems: mechanically activated fly ash and fly ash-blast furnace slag blends. Procedia Eng 108:231–238. https://doi.org/10.1016/j.proeng.2015.06.142
106. Vázquez-Rodríguez F, Elizondo N, Montes-González M et al (2023) Microstructural and mechanical characteristics of alkali-activated binders composed of milled fly ash and granulated blast furnace slag with μ-limestone addition. Materials. https://doi.org/10.3390/ma16103818
107. Zhang DW, Zhao KF, Wang DM, Li H (2021) Relationship of amorphous gel-microstructure-elastoviscosity properties of alkali-activated materials fresh pastes with different Ms waterglass. Constr Build Mater 14(287):123023
108. Mishra A, Lahoti M (2023) Effect of sodium hydroxide concentration on EAFS based alkali activated binder. Mater Today Proc. https://doi.org/10.1016/j.matpr.2023.03.717
109. Feng Y, Xue Z, Zhang B et al (2023) Effects of phosphogypsum substitution on the performance of ground granulated blast furnace slag/fly ash-based alkali-activated binders. J Build Eng 70:106387. https://doi.org/10.1016/j.jobe.2023.106387
110. Chen B (2023) Utilization of MSWI bottom ash as a mineral resource for construction materials. Dissertation, TU Delft. https://doi.org/10.4233/uuid:0793986f-b875-4693-a0f9-568978f2d632